PHYSICAL REVIEW B **112**, 205415 (2025)

Modeling g factors, hyperfine interaction, and optical properties of semiconductor quantum dots: Atomistic and eight-band $\boldsymbol{k}\cdot\boldsymbol{p}$ approaches

Krzysztof Gawarecki,[1,*] Alina Garbiec,[1] Jakub Stanecki,[1,2] and Michał Zieliński[3]
[1]*Institute of Physics, Wroclaw University of Science and Technology, Wybrzeże Wyspiańskiego 27, 50-370 Wrocław, Poland*
[2]*Faculty of Physics, University of Warsaw, ul. Pasteura 5, 02-093 Warszawa, Poland*
[3]*Institute of Physics, Faculty of Physics, Astronomy and Informatics, Nicolaus Copernicus University,*
ul. Grudziadzka 5, 87-100 Toruń, Poland

(Received 2 July 2025; revised 4 October 2025; accepted 23 October 2025; published 13 November 2025)

We present a detailed comparative study of two important theoretical approaches: atomistic $sp^3d^5s^*$ tight-binding and continuum eight-band $k\cdot p$ methods, for modeling the spin and optical properties of quantum dots (QDs). Our investigation spans key physical observables, including single-particle energy levels, g factors, exciton radiative lifetimes, and hyperfine-induced Overhauser field fluctuations. We perform our calculations for self-assembled InGaAs/GaAs QD systems as representative case studies. While both methods yield qualitatively consistent trends, quantitative discrepancies arise due to the different treatment of atomistic details, strain effects, and confinement. We introduce targeted corrections to the eight-band $k\cdot p$ framework, including a modified deformation potential scheme and adjusted remote-band contributions. Furthermore, we validate the eight-band implementation of hyperfine interactions by benchmarking it against the tight-binding model, showing reasonable convergence for both electrons and holes.

DOI: 10.1103/vjrj-jc3c

I. INTRODUCTION

Semiconductor quantum dots (QDs) have attracted significant attention due to their exceptional optical properties. Among them, GaAs/AlGaAs and InGaAs/GaAs QDs have been established as highly efficient single-photon sources, often outperforming alternative platforms in terms of emission brightness and purity [1–3]. Moreover, coupled QD systems have been proposed as a viable route to the generation of highly entangled photonic cluster states [4], which are essential resources for memory-free quantum computation and quantum communication.

Accurate theoretical modeling plays a crucial role in guiding the design and optimization of QD-based photonic and spintronic devices. Two primary frameworks are widely employed for simulating the electronic, spin, and optical properties of QDs: the multiband $\boldsymbol{k}\cdot\boldsymbol{p}$ method and atomistic tight-binding (TB) models. While both approaches have demonstrated considerable predictive power, they are based on fundamentally different assumptions, leading to distinct advantages, limitations, and domains of applicability.

The Landé g factor is a fundamental parameter governing the spin response of charge carriers in a magnetic field. Precise knowledge of the electron and hole g factors is critical for the design of spin-based quantum devices. For instance, a near-zero electron g factor, which suppresses Zeeman splitting between spin-up and spin-down states, enables the realization of quantum repeaters [5], while a large hole g factor, lifting the valence band degeneracy, is advantageous for spin initialization and the transfer of quantum information [6]. Furthermore, mismatches in g factors between coupled QDs introduce a pure spin-dephasing channel [7], and pose challenges for the deterministic generation of photonic cluster states [4].

Importantly, g factors in QDs can deviate substantially from their bulk counterparts [8] due to quantum confinement and strain, both of which are strongly influenced by the QD's geometry and material composition [9–12]. This makes accurate modeling indispensable. The g factors in self-assembled QDs have been extensively investigated in both experimental [11,13–17] and theoretical studies, using either multiband $\boldsymbol{k}\cdot\boldsymbol{p}$ models [11,12,18–20] or tight-binding approaches [21,22]. However, these methods often yield quantitatively different results due to their distinct physical assumptions and approximations.

The neutral excitons and excitonic complexes in QD systems were extensively studied in many works [13,23–27]. The exciton lifetime is a key parameter that governs the optical response of quantum dots, influencing both emission dynamics and coherence properties. Accurately determining this quantity is therefore essential for understanding and optimizing QD-based light sources. Within the dipole approximation, one can calculate the optical spectra [27–32] and exciton decay rates [25,33–35], providing insight into radiative recombination mechanisms.

The oscillator strength and optical transitions in QDs have been modeled using both the eight-band $\boldsymbol{k}\cdot\boldsymbol{p}$ framework [27,28,34,35] and tight-binding approaches [29–32]. These calculations typically rely on evaluating either momentum or position matrix elements, each of which involves specific assumptions regarding wavefunction representations and

---

[*] Contact author: Krzysztof.Gawarecki@pwr.edu.pl

boundary conditions. Given the methodological differences between these two classes of models, a systematic comparison of their predictions is highly desirable.

Electron and hole spins in quantum dots interact with the surrounding nuclear spin bath via the hyperfine interaction, which constitutes a primary source of decoherence and poses a fundamental limitation for utilizing InGaAs QDs in quantum information processing. Due to their negligible s-orbital character, hole states couple more weakly to nuclear spins [36], enabling significantly longer coherence times compared to their electron counterparts [37,38].

Theoretical modeling of hyperfine coupling in QDs often relies on simplified descriptions of carrier wavefunctions [39]. One of the more refined approaches was introduced in Ref. [40], where the hyperfine Hamiltonian was formulated within the eight-band $\boldsymbol{k}\cdot\boldsymbol{p}$ framework. However, since the $\boldsymbol{k}\cdot\boldsymbol{p}$ method is inherently a continuum model, approximating atomistic interactions requires a series of assumptions. In this scheme, Bloch functions were expanded in terms of hydrogen-like atomic orbitals, with wavefunction localization on cation and anion sites inferred from empirical considerations. Moreover, d-orbital contributions, which play a crucial role for holes [41], were included through a constant weighting factor, the accuracy of which is subject to considerable uncertainty. In contrast, the $sp^3d^5s^*$ tight-binding model offers a natural platform for atomistic simulations. It inherently accounts for the orbital composition and spatial distribution of the wavefunction across atomic sites, including d-orbital admixture. As a result, the TB-based description of hyperfine interaction is more direct and less dependent on empirical parameters, making it a suitable benchmark for evaluating the approximations introduced in the $\boldsymbol{k}\cdot\boldsymbol{p}$ framework as implemented in Ref. [40]. We also note, that the tight-binding model has been utilized in the description of hyperfine interaction for transition metal dichalcogenides [42].

In this work, we present a systematic comparison of modeling approaches used to describe the spectral and spin-related properties of quantum dots. Specifically, we calculate energy levels, exciton lifetimes, electron and hole g factors, and hyperfine-induced Overhauser fields for InGaAs/GaAs QDs using both eight-band $\boldsymbol{k}\cdot\boldsymbol{p}$ and $sp^3d^5s^*$ tight-binding models. In addition, we propose targeted refinements to the eight-band $\boldsymbol{k}\cdot\boldsymbol{p}$ framework that improve its predictive performance, particularly for energy levels and g factor values. With these enhancements, we achieve close agreement between the carrier energies obtained from the atomistic and continuum approaches. We also demonstrate that both modeling techniques yield consistent trends for g factors and Overhauser field fluctuations, with reasonably good quantitative agreement. However, for exciton lifetimes, we observe some discrepancies between the two methods, depending on the indium composition and structural parameters of the quantum dot.

The paper is organized as follows. In Sec. II, we describe the morphology of the quantum dots under investigation and outline the model used to account for strain effects. Sections III and IV present the $sp^3d^5s^*$ tight-binding and eight-band $\boldsymbol{k}\cdot\boldsymbol{p}$ models, respectively. The theoretical framework for exciton states and radiative lifetimes is detailed in Sec. V, while the hyperfine interaction and Overhauser field fluctuations are addressed in Sec. VI. The results of our numerical simulations, along with a comparative discussion, are presented in Sec. VII. A summary of the main findings is provided in Sec. VIII, and additional computational details are given in the Appendix.

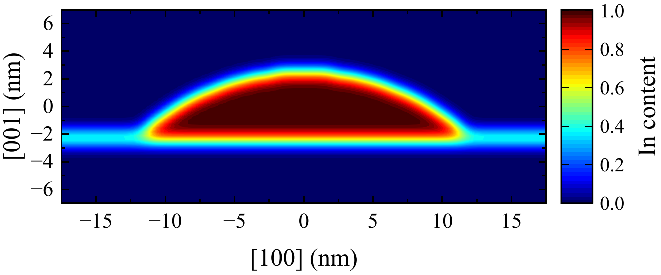

FIG. 1. Composition distribution for the InGaAs/GaAs QD.

II. STRUCTURE GEOMETRY AND STRAIN MODEL

The calculations are performed for a single self-assembled InGaAs/GaAs QD. We represent the QD geometry by the dome shape of height h (if not stated otherwise, it is 8 lattice constants a) and the radius (at the base) $r = 21a$. We assume a circular shape of the QD, which is subjected to the underlying atomic lattice breaking the exact axial symmetry. The dot is placed on a wetting layer of thickness a (the single lattice constant). The material distribution is presented in Fig. 1. For simplicity, we assume a constant $\mathrm{In}_x\mathrm{Ga}_{1-x}\mathrm{As}$ distribution (denoted as x_{QD}) in the QD and in the wetting layer. To take into account the material intermixing at the interfaces, the initial composition is processed by the Gaussian blur with a standard deviation of a. As can be seen in Fig. 1, this intermixing leads to a pronounced reduction of the In content in the wetting layer (by “leaking” In atoms to the barrier).

The strain arising due to the lattice mismatch between InAs and GaAs is found within Martin’s valence force field (VFF) model [43,44]. The optimal atomic positions that minimize the elastic energy of the system are found numerically. The model and calculation details are described in Appendix 1.

We also include the effect of the piezoelectric field with the polarization taken up to the second order in strain tensor elements [45]. The parameters are taken from Ref. [46].

III. THE TIGHT-BINDING MODEL

To calculate the electron and hole states in the atomistic way, we performed simulations within the $sp^3d^5s^*$ TB model [47] in the nearest neighbor approximation. The second quantization Hamiltonian can be written as

$$H^{(\mathrm{TB})} = H^{(\mathrm{TB})}_{\mathrm{diag}} + H^{(\mathrm{TB})}_{\mathrm{t}} + H^{(\mathrm{TB})}_{\mathrm{so}} + H^{(\mathrm{TB})}_{\mathrm{S},\boldsymbol{B}} + H^{(\mathrm{TB})}_{\mathrm{L},\boldsymbol{B}},$$

where

$$H^{(\mathrm{TB})}_{\mathrm{diag}} = \sum_{i}^{N_{\mathrm{A}}} \sum_{\alpha} E^{(i)}_{\alpha} a^{\dagger}_{i,\alpha} a_{i,\alpha}, \tag{1}$$

$$H^{(\mathrm{TB})}_{\mathrm{t}} = \sum_{i}^{N_{\mathrm{A}}} \sum_{j\neq i}^{N_{\mathrm{A}}} \sum_{\alpha,\beta} t^{(ij)}_{\alpha\beta} e^{i\Theta_{ij}} a^{\dagger}_{i,\alpha} a_{j,\beta}, \tag{2}$$

$$H_{\mathrm{so}}^{(\mathrm{TB})} = \sum_{i}^{N_{\mathrm{A}}} \sum_{\alpha,\beta} \Delta_{\alpha\beta}^{(i)} a_{i,\alpha}^{\dagger} a_{i,\beta}, \tag{3}$$

$$H_{\mathrm{S},\boldsymbol{B}}^{(\mathrm{TB})} = g_0 \frac{\mu_B}{\hbar} \sum_{i}^{N_{\mathrm{A}}} \sum_{\alpha,\beta} [(S_x)_{\alpha\beta} B_x + \mathrm{c.p.}] a_{i,\alpha}^{\dagger} a_{i,\beta}, \tag{4}$$

$$H_{\mathrm{L},\boldsymbol{B}}^{(\mathrm{TB})} = \frac{\mu_B}{\hbar} \sum_{i}^{N_{\mathrm{A}}} \sum_{\alpha,\beta} [(L_x)_{\alpha\beta} B_x + \mathrm{c.p.}] a_{i,\alpha}^{\dagger} a_{i,\beta}, \tag{5}$$

where N_{A} is the number of atoms in the system, $E_{\alpha}^{(i)}$ is the on-site energy for the orbital α (the index includes also spin) localized at the ith atom; $a_{i,\alpha}^{\dagger}$, $a_{i,\alpha}$ are the electron creation and annihilation operators, respectively; $t_{\alpha\beta}^{(ij)}$ are hopping integrals for a given pair of atoms and orbitals; $\Delta_{\alpha\beta}^{(i)}$ is a matrix element of the spin-orbit coupling; "c.p." denotes cyclic permutations of x, y, z indices.

The magnetic field $\boldsymbol{B}$ enters the model, in a gauge-invariant form, via Peierls substitution and the Zeeman terms [48–50]. The Peierls substitution introduces the magnetic vector potential via a phase shift of the tight-binding nearest-neighbor-hopping parameters in $H_{\mathrm{t}}^{(\mathrm{TB})}$. For a constant magnetic field and the symmetric gauge [50]

$$\theta_{ij} = \frac{e}{2\hbar} \boldsymbol{B} \cdot (\boldsymbol{R}_i \times \boldsymbol{R}_j),$$

where $\boldsymbol{R}_i$ is the position of the ith atom.

When spin is incorporated into the modeling, intra-atomic matrix elements should be augmented by the spin Zeeman terms [48], along with the atomic orbital angular momentum Zeeman terms that—in principle—should be accounted for on equal footing [51]. The spin Zeeman term is represented by the $H_{\mathrm{S},\boldsymbol{B}}^{(\mathrm{TB})}$, where μ_B is the Bohr magneton, $g_0 = 2$, and $(S_n)_{\alpha\beta}$ are the matrix elements of the spin operator. The interaction with atomic-orbital angular momentum is also included in the Hamiltonian via $H_{\mathrm{L},\boldsymbol{B}}^{(\mathrm{TB})}$, where $(L_n)_{\alpha\beta}$ are the orbital angular momentum matrix elements. Here, the following approximations were made: we keep the on-site terms only, neglecting the interatomic elements, which should already be accounted for by the Peierls term. We also assume that atomic orbitals transform like spherical harmonics, although in a crystal, the symmetry of orthogonalized orbitals is reduced [52]. The rationale behind this approach is to avoid any fitting parameters or introduction of an *ad hoc* basis, and aim for a better description of an isolated atom where both Zeeman terms due to spin and atomic-orbital angular momentum should not be neglected. The explicit expressions for $(L_n)_{\alpha\beta}$ are given in Appendix 2.

Following Ref. [53], the impact of strain enters the model threefold ways: by altering the bond angles, via the scaling factors (the generalized Harrison law), and by diagonal corrections to the d shell on-site energies. We note that more advanced schemes have been proposed [54,55], but their implementation is outside the scope of our paper.

We transform the Hamiltonian of Ref. [47] to the angular momentum basis $\{s, p_{-1}, p_0, p_1, d_{-2}, d_{-1}, d_0, d_1, d_2, s^*\}$ with two spin configurations (20 basis states in total). In this basis, the single-particle states are expressed as

$$|\psi_\lambda\rangle = \sum_{\alpha} \sum_{i}^{N_{\mathrm{A}}} w_{i,\alpha}^{(\lambda)} |\boldsymbol{R}_i; \alpha\rangle, \tag{6}$$

where $w_{i,\alpha}^{(\lambda)}$ are complex coefficients, i denotes the atomic site, and α is the orbital.

The material parameters for InAs and GaAs are taken from Ref. [53]. The more technical details related to the model implementation are given in Ref. [56] and in Appendix of Ref. [32].

IV. EIGHT-BAND $K \cdot P$ MODEL

A. Bulk Hamiltonian

We performed simulations within the eight-band $k \cdot p$ model, which is a well-established theoretical description. The model takes into account the lowest conduction band block $\Gamma_{6\mathrm{c}}$, the valence band block containing the heavy/light-hole (HH/LH) subbands ($\Gamma_{8\mathrm{v}}$), and the spin-orbit split-off band block $\Gamma_{7\mathrm{v}}$. The kinetic part of the Hamiltonian in the invariant expansion form is given by [57,58]

$$\begin{aligned}
H_{6\mathrm{c}6\mathrm{c}}^{(\mathrm{k})} &= \left(E_g + \frac{\hbar^2}{2m_0} A' k^2\right) \mathbb{I}, \\
H_{8\mathrm{v}8\mathrm{v}}^{(\mathrm{k})} &= -\frac{\hbar^2}{2m_0} \gamma_1' k^2 \mathbb{I} + \frac{\hbar^2}{2m_0} \left\{ 2\gamma_2' \left(J_x^2 - \frac{1}{3} J^2\right) k_x^2 \right. \\
&\quad \left. + 4\gamma_3' \{J_x, J_y\}\{k_x, k_y\} + \mathrm{c.p.} \right\} \\
&\quad + \frac{2}{\sqrt{3}} C_{\mathrm{k}} \left[\left\{ J_x, J_y^2 - J_z^2 \right\} k_x + \mathrm{c.p.} \right], \\
H_{7\mathrm{v}7\mathrm{v}}^{(\mathrm{k})} &= -\left(\Delta_0 + \frac{\hbar^2}{2m_0} \gamma_1' k^2\right) \mathbb{I}, \\
H_{8\mathrm{v}7\mathrm{v}}^{(\mathrm{k})} &= \frac{3\hbar^2}{m_0} \left[\gamma_2' T_{xx}^{\dagger} k_x^2 + 2\gamma_3' T_{xy}^{\dagger} \{k_x, k_y\} + \mathrm{c.p.} \right] \\
&\quad - i\sqrt{3} C_{\mathrm{k}} (T_{yz}^{\dagger} k_x + \mathrm{c.p.}), \\
H_{6\mathrm{c}8\mathrm{v}}^{(\mathrm{k})} &= \sqrt{3} P \eta (T_x k_x + \mathrm{c.p.}), \\
H_{6\mathrm{c}7\mathrm{v}}^{(\mathrm{k})} &= -\frac{1}{\sqrt{3}} P \eta (\sigma_x k_x + \mathrm{c.p.}),
\end{aligned} \tag{7}$$

where E_g is the band gap, C_{k} is the parameter related to the inversion asymmetry, A' and γ_{1-3}' (the modified Luttinger parameters) account for the remote band contributions, m_0 is the free electron mass, Δ_0 is the splitting between $\Gamma_{8\mathrm{v}}$ and $\Gamma_{7\mathrm{v}}$ bands due to the spin-orbit coupling. P is a parameter proportional to the interband momentum matrix element, which is related to the Kane energy (E_{P}) by $P = \sqrt{E_{\mathrm{P}} \hbar^2/(2m_0)}$. Here we introduce η—a dimensionless scaling factor, whose meaning will be explained further in the text. The $\mathbb{I}$ is the unit matrix (of the proper size), J_i are the total angular momentum matrices (4×4) for $j = 3/2$, $J^2 = J_x^2 + J_y^2 + J_z^2$, T_i are (2×4) matrices connecting $\Gamma_{6\mathrm{c}}$ and $\Gamma_{8\mathrm{v}}$ blocks, and $T_{ij} = T_i J_j + T_j J_i$. We also take into account perturbative SO terms (the Dresselhaus spin-orbit coupling) described in Refs. [12,57].

As the $E_{\rm P}$ values for InAs and GaAs break the ellipticity of the resulting differential equations [59], we use the reduced values of $E_{\rm p}^{(\rm red)}$ (see Appendix 3).

B. Effect of strain

When a crystal undergoes deformation, its properties change, and symmetry may be reduced. A common approach to address this involves introducing "deformed" coordinates, which restore the periodicity of the crystal potential [60]. This includes transformations: $x_i \to \sum_j (\delta_{ij} + \epsilon_{ij}) x_j$, $k_i \to \sum_j (\delta_{ij} - \epsilon_{ij}) k_j$, and $p_i \to \sum_j (\delta_{ij} - \epsilon_{ij}) p_j$ in the initial $\boldsymbol{k}\cdot\boldsymbol{p}$ equation, where $\hat{\epsilon}$ is the strain tensor. Consequently, it leads to the appearance of multiple new terms in the Hamiltonian. The most important ones are proportional to ϵ_{ij} and weighted by the deformation potentials. They appear in the standard Bir-Pikus Hamiltonian, which contains strain tensor elements in linear order. However, in this paper, we utilize the second-order scheme [61,62], which was proven successful in InAs/GaAs systems [62]. Another category of strain-related terms exhibits proportional dependence on both k_i and ϵ_{jk}. We incorporate such terms as described in Refs. [57,63]. The important contributions of this kind to the Hamiltonian are

$$H_{6c8v}^{(\rm k,str)} = -2\sqrt{3}P\eta\left(T_x \sum_j \epsilon_{xj} k_j + \text{c.p.}\right),$$

$$H_{6c7v}^{(\rm k,str)} = \frac{2}{\sqrt{3}}P\eta\left(\sigma_x \sum_j \epsilon_{xj} k_j + \text{c.p.}\right).$$

These terms affect the g factor value [64] and spin-flip relaxation in quantum dots [65–69].

C. Envelope function approximation

To simulate the QD system, the envelope function approximation (EFA) is applied. The Hamiltonian is transformed into real space via the substitution $k_i = -i\partial/\partial x_i$. These are discretized according to the finite difference scheme. The details related to the implementation (e.g., the operator ordering) are given in Ref. [12]. Since in the present paper, strain is calculated in the atomistic way (Martin's VFF model), the strain tensor field is computed by interpolation into a regular mesh. Also, the piezoelectric field is implemented in this way.

Although the EFA $k\cdot p$ model is based on the continuous medium approximation, it is beneficial to use a mesh that matches the underlying atomic lattice. In particular, when the hyperfine interaction (a truly atomistic effect) is studied within the $k\cdot p$ theory [40], which is the case in the present paper. Consequently, we perform calculations on the uniform, rectangular grid with the size of $a \times a \times a/2$, where a is the barrier (GaAs) lattice constant.

However, the described approach has some limitations. Although initially (at the beginning of the strain calculations) the QD material is matched to the barrier, the strain relaxation leads to displacements that modify the QD shape. In the TB calculations, this effect is inherently taken into account, as the model relies on the positions of individual atoms. In contrast, in the $k\cdot p$ calculations, the numerical lattice is fixed (matched to the unstrained barrier material), and all displacements are represented via a strain tensor field. To improve the accuracy, while keeping the model simple, we introduce a scaling factor into the most important terms H_{6c8v}, H_{6c7v} containing k_i in the linear order. The scaling factor is

$$\eta(\boldsymbol{r}) = 1 - [a(\boldsymbol{r}) - a]/a, \tag{8}$$

where $a(\boldsymbol{r})$ is the lattice constant (in the sense of the virtual crystal approximation) of the material at a given point.

D. Magnetic field dependence

The effect of the magnetic field is taken into account using a gauge-invariant scheme [70], which is a rigorous implementation of the $\boldsymbol{k} \to \boldsymbol{k} + (e/\hbar)\boldsymbol{A}$ substitution for the discrete numerical grid. Here $\boldsymbol{A}$ is the vector potential. In the presence of the magnetic field $\boldsymbol{B}$, different components of $\boldsymbol{k}$ do not commute, giving

$$[k_n, k_m] = -i\frac{e}{\hbar}\sum_{l=x,y,z} \epsilon_{nml} B_l,$$

where ϵ_{nml} is the Levi-Civita symbol. The Hamiltonian part associated with the magnetic field is

$$H^{(\rm B)} = \frac{g_0 \mu_{\rm B}}{\hbar}\sum_i S_i^{(\rm kp)} B_i + H^{(\rm B,r)}.$$

The first term corresponds to the spin Zeeman part. In the eight-band $k\cdot p$, this enters with the block matrix [57]

$$S_i^{(\rm kp)} = \frac{\hbar}{2}\begin{pmatrix} \sigma_i & 0 & 0 \\ 0 & \frac{2}{3}J_i & -2T_i^\dagger \\ 0 & -2T_i & -\frac{1}{3}\sigma_i \end{pmatrix}.$$

The orbital Zeeman part (for the VB) and the remote-band contributions are represented by [57]

$$\begin{aligned}
H_{6c6c}^{(\rm B,r)} &= \tfrac{1}{2}\mu_B \bar{g}'[\sigma_z B_z + \text{c.p.}],\\
H_{8v8v}^{(\rm B,r)} &= -2\mu_B\big[\bar{\kappa}' J_z B_z + q' J_z^3 B_z + \text{c.p.}\big],\\
H_{7v7v}^{(\rm B,r)} &= -2\mu_B \bar{\kappa}'[\sigma_z B_z + \text{c.p.}],\\
H_{8v7v}^{(\rm B,r)} &= -3\mu_B \bar{\kappa}'[T_z^\dagger B_z + \text{c.p.}],\\
H_{7v8v}^{(\rm B,r)} &= H_{8v7v}^{(\rm B,r)\dagger},
\end{aligned}$$

where q' is an anisotropy parameter,

$$\bar{g}' = g - g_0 + \frac{2E_{\rm p}^{(\rm red)}\Delta_0}{3E_{\rm g}(E_{\rm g} + \Delta_0)}, \tag{9}$$

$$\bar{\kappa}' = \kappa + \frac{g_0}{6} - \frac{E_{\rm p}^{(\rm red)}}{6E_g}, \tag{10}$$

here g, κ are the target parameters for the conduction and valence band g factors, respectively.

While the above Hamiltonian is valid for a uniform material system, for a nanostructure composed of two (or more) different materials (such as self-assembled QDs), all the material constants are position dependent, and proper operator ordering must be taken into account [71,72]. For example, $\bar{g}' B_z \to i\hbar/e(k_x \bar{g}' k_y - k_y \bar{g}' k_x)$.

The drawback of the described model is the fact that Eqs. (9) and (10) contain the reduced value of $E_{\rm p}^{(\rm red)}$. Consequently, the impact of the bulk values of g and κ on the results is still considerable. As these bulk values do not contain the strain and confinement effects, they reduce the overall accuracy. The problem is particularly important for $\bar{g}'$, as the formula contains $\propto E_{\mathrm{g}}^2$ in the denominator. To improve the model, we propose the following modification of Eq. (9)

$$\bar{g}' = g - g_0 + \frac{2E_{\mathrm{p}}\Delta_0}{3E_{\mathrm{g}}(E_{\mathrm{g}}+\Delta_0)} - \frac{2\big(E_{\mathrm{p}} - E_{\mathrm{p}}^{(\mathrm{red})}\big)\Delta_0}{3\widetilde{E}_{\mathrm{g}}(\widetilde{E}_{\mathrm{g}}+\Delta_0)}, \tag{11}$$

where $\widetilde{E}_{\mathrm{g}}$ is the modified energy gap with the major hydrostatic strain contribution, i.e., $\widetilde{E}_{\mathrm{g}} = E_{\mathrm{g}} + (a_{\mathrm{c}} - a_{\mathrm{v}})(\epsilon_{xx} + \epsilon_{yy} + \epsilon_{zz})$. To avoid introducing anisotropic corrections, we do not consider here the HH-LH splitting due to strain. Another reasonable approach would be to take $\widetilde{E}_{\mathrm{g}}$ as the energy difference between the lowest electron and hole states in the QD. In such a case, the simulations would be performed in a self-consistent manner, but this will not be the case in the present paper.

V. EXCITON STATES AND LIFETIMES

We calculate the neutral exciton states within the configuration-interaction (CI) approach. The standard Hamiltonian expressed in the second quantization manner is [31,73]

$$H^{(\mathrm{CI})} = \sum_i E_i^{(\mathrm{e})} a_i^\dagger a_i + \sum_j E_j^{(\mathrm{h})} h_j^\dagger h_j - \sum_{ii'jj'} V_{ijj'i'} a_i^\dagger h_j^\dagger h_{j'} a_{i'}, \tag{12}$$

where $E_i^{(\mathrm{e/h})}$ are the electron/hole single-particle energies; $a_i^\dagger$ (a_i) and $h_i^\dagger$ (h_i) are the electron and hole creation (annihilation) operators; $V_{ijj'i'}$ are the electron-hole Coulomb matrix elements. The details of the calculations for the Coulomb matrix elements $V_{ijj'i'}$ are given in Appendix 4. As we are interested here in the lifetimes of the neutral exciton states, we neglect the exchange terms and multielectron (and multihole) interactions. The nth exciton state can be written as

$$|X_n\rangle = \sum_i^{n_e}\sum_j^{n_h} c_{ij}^{(n)} a_i^\dagger h_j^\dagger |\mathrm{vac.}\rangle,$$

where $c_{ij}^{(n)}$ are complex coefficients resulting from the diagonalization of $H^{(\mathrm{CI})}$; n_e, n_h are the numbers of electron and hole states in the single-particle basis; and $|\mathrm{vac.}\rangle$ is the vacuum state.

The interaction with light is introduced in terms of the dipole approximation [31,74]. For deeper insight and further comparison, we consider two formulations based on the position and momentum operators, namely,

(1) the oscillator strength of the exciton state $|X_n\rangle$ is calculated from

$$f_n = \frac{2m_0}{\hbar^2 e^2} E_n^{(\mathrm{X})} \sum_{\mu=x,y,z} |\langle \mathrm{vac.}|D_\mu|X_n\rangle|^2,$$

where

$$\boldsymbol{D} = \sum_{i,j} \boldsymbol{d}_{ij}\, h_i a_j,$$

giving

$$f_n = \frac{2m_0}{\hbar^2 e^2} E_n^{(\mathrm{X})} \sum_{\mu=x,y,z} \left| \sum_{i,j} c_{ji}^{(n)} (d_\mu)_{ij} \right|^2, \tag{13}$$

where $\boldsymbol{d}_{ij} = -e\boldsymbol{x}_{ij}$ with the matrix elements of the position operator

$$\boldsymbol{x}_{ij} = \sum_{n,m}\sum_{\alpha,\beta} w_{n,\alpha}^{(i)*} w_{m,\beta}^{(j)} \langle \boldsymbol{R}_n;\alpha|\boldsymbol{x}|\boldsymbol{R}_m;\beta\rangle.$$

Here, the indices n, m go over atoms and α, β over the orbitals. The $\boldsymbol{x}_{ij}$ elements are calculated directly, neglecting the orbital-dependent (the basis-dependent) terms, i.e.,

$$\langle \boldsymbol{R}_n;\alpha|\boldsymbol{x}|\boldsymbol{R}_m;\beta\rangle \approx \boldsymbol{R}_n \delta_{\alpha\beta}\delta_{mn}. \tag{14}$$

We note here that this approach neglects contributions from local, interatomic terms. This is due to enlarging a model with position parameters may lead to errors due to incompleteness [49].

(2) The oscillator strength of $|X_n\rangle$ is calculated from [34,75]

$$f_n = \frac{2}{m_0 E_n^{(\mathrm{X})}} \sum_{\mu=x,y,z} \left| \sum_{i,j} c_{ji}^{(n)} (p_\mu)_{ij} \right|^2, \tag{15}$$

The $\boldsymbol{p}_{ij}$ momentum matrix elements are calculated using the Hellman-Feynman theorem [56,76,77], which gives

$$\boldsymbol{p}_{ij} = \frac{im_0}{\hbar} \sum_{n,m}\sum_{\alpha,\beta} w_{n,\alpha}^{(i)*} w_{m,\beta}^{(j)} \left(\boldsymbol{R}_m - \boldsymbol{R}_n\right) t_{\alpha\beta}^{(nm)}. \tag{16}$$

In the calculation of $\boldsymbol{x}_{ij}$ and $\boldsymbol{p}_{ij}$, the valence-band states are represented in the electron picture–not in the hole picture as in the other parts of the paper.

Finally, the exciton lifetime is given by [34,78]

$$\tau_n = \frac{6\pi\epsilon_0 m_0 c^3 \hbar^2}{n_r\big(E_n^{(\mathrm{X})}/\hbar\big)\big(E_n^{(\mathrm{X})}\big)^2 f_n e^2},$$

where $n_r(\omega)$ is the frequency-dependent refractive index of the barrier material (here GaAs) [79], explicitly given in Appendix 4.

VI. THE HYPERFINE INTERACTION

The interaction of the carrier (electron or hole) with nuclei is given by the Hamiltonian [40,41,80]

$$H^{(\mathrm{hf})} = \sum_n \boldsymbol{A}(\boldsymbol{r} - \boldsymbol{R}_n)\cdot\boldsymbol{\mu}_n,$$

where the index n goes over all nuclei, $\boldsymbol{\mu}_n = \zeta_n \mu_N \boldsymbol{I}_n$ is the magnetic moment for a given nucleus, ζ_n is a dimensionless parameter, μ_N is the nuclear magneton, and the nuclear spin is $\hbar\boldsymbol{I}_n$. The (pseudo)vector quantity $\boldsymbol{A}$ is given by

$$\boldsymbol{A}(\boldsymbol{r}) = \frac{\mu_0\mu_B}{2\pi\hbar}\left(\frac{8\pi}{3}\delta(\boldsymbol{r})\boldsymbol{S} + \frac{\boldsymbol{L}}{r^3} + \frac{3(\hat{\boldsymbol{r}}\cdot\boldsymbol{S})\hat{\boldsymbol{r}} - \boldsymbol{S}}{r^3}\right),$$

where μ_0 is the vacuum permeability, $\boldsymbol{S}$ is the spin operator, $\boldsymbol{L}$ is the angular momentum operator, and $\hat{\boldsymbol{r}}$ is the unit vector. The first term in the bracket is the contact term, the second

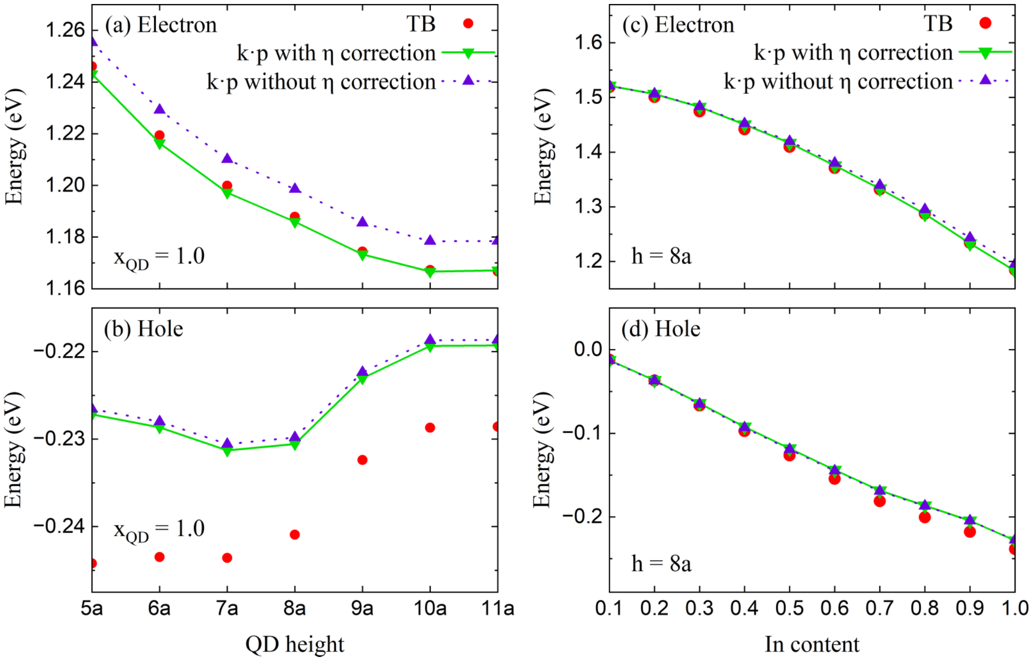

FIG. 2. The electron and hole energy dependence on the QD height (a), (b) and the QD composition (c), (d). For the height dependence [(a) and (b)], the QD composition is fixed to $x_{\mathrm{QD}} = 1.0$. In the composition dependence [(c) and (d)], the height is fixed to $h = 8a$.

one describes the coupling between the nuclear spin and the orbital angular momentum, and finally, the last term describes the hyperfine dipole interaction.

To calculate the Overhauser field $\boldsymbol{h}$ for the lowest Zeeman doublet of the electron or hole states, one needs to project the Hamiltonian $H^{(\mathrm{hf})}$ into the two-dimensional subspace of these states

$$H^{(\mathrm{hf})} = \tfrac{1}{2}\boldsymbol{h}\cdot\tilde{\boldsymbol{\sigma}},$$

where $\tilde{\boldsymbol{\sigma}}$ is the vector of the Pauli matrices (related to the subspace of the considered states). This leads to the form [40]

$$\begin{aligned} H^{(\mathrm{hf})} &= \frac{1}{2}\sum_j \mathrm{Tr}\{H^{(\mathrm{hf})}\tilde{\sigma}_j\}\tilde{\sigma}_j \\ &= \frac{1}{2}\sum_n\sum_{i,j}\left(\mathcal{H}^{(n)}_{ij} I_{n,i}\right)\tilde{\sigma}_j, \end{aligned}$$

where

$$\mathcal{H}^{(n)}_{ij} = \mu_N \zeta_n \mathrm{Tr}\{A_i(\boldsymbol{r}-\boldsymbol{R}_n)\tilde{\sigma}_j\}.$$

The fluctuations of the Overhauser field are then given by the mean square components [40]

$$\langle h_j^2\rangle = \frac{1}{3}\sum_n I_n(I_n+1)\sum_i \left(\mathcal{H}^{(n)}_{ij}\right)^2, \qquad (17)$$

where we assume that nuclei are in an unpolarized thermal state.

The implementation for the eight-band $k\cdot p$ Hamiltonian is described in detail in Ref. [40]. In such a case, the wave functions need to be adapted for atomic-oriented hyperfine calculations. This is done by expressing the Bloch functions in terms of the hydrogenlike orbitals. Owing to its initial continuous, nonatomic design, the model relies on several fundamental assumptions. In particular, the coefficients describing the spread of the wave functions on anions (As) and cations (In, Ga) were introduced. Also, the admixture of the d-type orbitals is described in terms of the external parameter.

In contrast to the $k\cdot p$ formulation, the tight-binding binding approach provides information about the wave function localization on individual atomic nodes. Furthermore, the tight-binding model in its $sp^3d^5s^*$ version inherently describes also the d orbitals, which are crucial for the hole-nucleus coupling. The details of our TB implementation are given in Appendix 5.

VII. RESULTS

This section provides a systematic analysis of the outcomes produced by various models, each utilizing a distinct level of approximation. We focus on the results of the single-particle energies, electron and hole g factors, exciton lifetimes, and the Overhauser field.

A. Energy levels

We calculated the electron and hole single-particle energy levels within the tight-binding and $k\cdot p$ models. The energy dependence on the QD height is shown in Figs. 2(a) and 2(b). As can be expected, the electron energy decreases with increasing QD size. We can also see that the results of both classes of models are in good agreement. However, there is a systematic shift in the electron energy between the TB and the $k\cdot p$, where the latter gives higher energy on the order of a dozen meV. The reason can be related to the barrier-matched numerical grid, as described in Sec. IV C, which can be refined

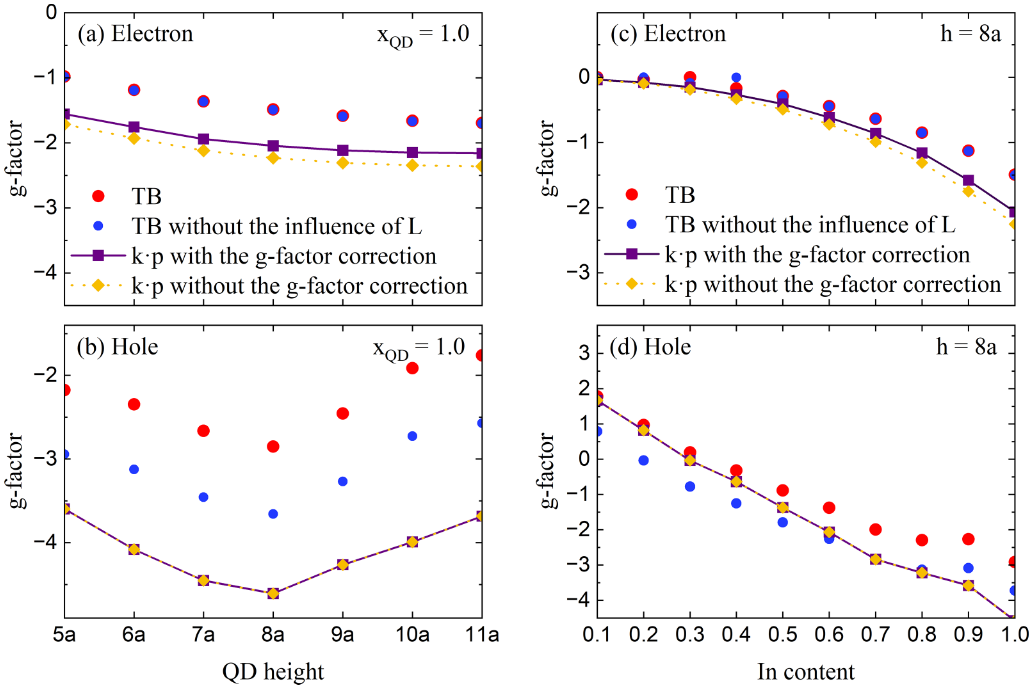

FIG. 3. The electron and hole *g* factor dependence on the QD height [(a) and (b)] and the QD composition [(c) and (d)]. For the height dependence [(a) and (b)], the QD composition is fixed to $x_{\mathrm{QD}} = 1.0$. In the composition dependence [(c) and (d)], the height is fixed to $h = 8a$.

by introducing the η factor. As shown in Fig. 2(a), in such a case, the accuracy of the $k\cdot p$ model is improved.

In the case of the hole [Fig. 2(b)], the energy dependence is more complicated, which results from the overall sensitivity of the hole states on the strain distribution. The latter strongly depends on the QD aspect ratio [81], which is affected by the changing height. In contrast to the electron, the η correction introduces only a minor shift. This is due to the difference between the electron and hole effective masses (which govern their sensibilities on the confinement). Therefore the energy shift between the $k\cdot p$ and TB models for hole has a different origin, and it is likely that it is related to the shear strain [62].

In principle, for growing QD size, the results should tend to the bulk case, where the two methods are consistent. However, even for the tallest QD (the height of the 11 lattice constants), we are far from this limit. In addition, increasing the QD dome aspect ratio leads to stronger shear strain, in which regime the agreement between the methods decreases [62].

We also studied the energies as a function of the QD composition $\mathrm{In}_x\mathrm{Ga}_{1-x}\mathrm{As}$. The results are shown in Figs. 2(c) and 2(d). As in the previous case, we observe an overall good agreement between the models. Both models consistently treat nonlinearities in the energy dependence, which was achieved by tuning the bowing parameter of the band gap in the $k\cdot p$. Also here, the η correction considerably improves the accuracy of the $k\cdot p$ model for the electron energy levels.

B. Electron and hole *g* factors

The electron and hole *g* factors were calculated using the tight-binding and the $k\cdot p$ approaches. The absolute value of a *g* factor results from the Zeeman energy splitting, while its sign is determined from the spin orientations of states

$$g_{c/v} = \frac{\left|E_2^{(c/v)} - E_1^{(c/v)}\right|}{\mu_B|\boldsymbol{B}|}\,\mathrm{sgn}\left(\sum_{i=x,y,z} B_i\langle J_i\rangle_2\right),$$

where $E_1^{(c/v)}$ and $E_2^{(c/v)}$ are the energies of the two lowest states (the c and v means the conduction-band and valence-band states, respectively), sgn() is the signum function, $\langle J_i\rangle_2 = \langle\Psi_2|\hat{J}_i|\Psi_2\rangle$ is the average of the ith component of the total angular momentum in the excited state of the Zeeman doublet. We consider here the magnetic field oriented along the z direction (the Faraday orientation). Note that there are various sign conventions for the hole *g* factor [72]. Here we take $g_h = -g_v$, consistently to Ref. [12].

The numerical results for the *g* factors are shown in Fig. 3. They differ significantly from the bulk TB values, which for the electron *g* factor are −14.18 in InAs, and −0.066 in GaAs; and for the hole *g* factor: −44.17 in InAs and −9.51 in GaAs. This difference is the effect of strain and quantum confinement [82,83]. The value of the electron *g* factor [Fig. 3(a)] gets slightly closer to the bulk value with increasing QD height, which is related to decreasing energy gap (due to a weaker confinement) in the Roth formula [8,82]. For the hole, the situation becomes more complicated, and we can see nonmonotonic dependence [Fig. 3(b)]. One should note that hole properties are very sensitive to the strain distribution, which governs the degree of heavy-light-hole mixing and opens some channels of the spin-orbit coupling [12,57]. In fact, the biaxial and shear strain crucially depend on the QD aspect ratio, which changes with the QD height.

The dependence of the electron and hole *g* factors on the QD composition [Figs. 3(c) and 3(d)] is monotonic up to some deviations which can result from random alloying. The abso-

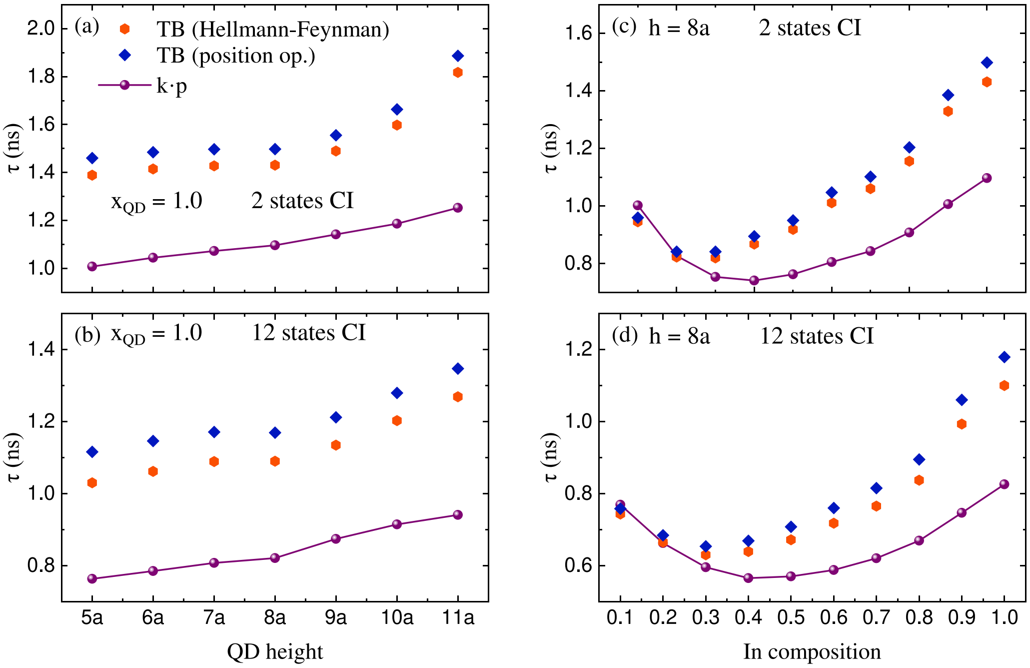

FIG. 4. The radiative lifetime dependence on the QD height (a), (b) and the QD composition [(c) and (d)]. For the blue points, the oscillator strength is calculated using the position matrix elements [Eq. (13)], and for the red points we used the momentum matrix elements [Eq. (15)]. The results in (a) and (c) are obtained for the CI basis of 2 electron and 2 hole states; and (b) and (d) present the ones for 12 states of each type.

lute value of the electron g factor is strongly reduced for small In content, which results from small bulk GaAs value (−0.066 predicted by the TB, which deviates from the experimental value of −0.44). In the case of the hole, the g factor changes its sign for the QD material of about $\mathrm{In}_{0.4}\mathrm{Ga}_{0.6}\mathrm{As}$.

One can see that the contribution from the orbital angular momentum significantly changes the values (see the TB results) of the hole g factor. The effect for the electron is small, which can be expected owing to its (mainly) s-type atomic orbital character.

While the TB and $k\cdot p$ models consistently predict trends, the values from the latter are typically larger (in their absolute value). This can be partially related to the limited size of the basis in the eight-band $k\cdot p$ model compared to the $sp^3d^5s^*$ tight-binding model. The other reason can be related to the impact of the remote band contributions, which are calculated from the bulk values (hence, do not account for the effect of strain and confinement). As shown in Figs. 3(a) and 3(c), this can be improved to some degree via the correction introduced in Eq. (11).

C. Exciton lifetimes

The exciton lifetimes calculated as a function of the QD height and the In content are shown in Figs. 4(a), 4(b) and 4(c), 4(d), respectively. One can see that increasing the height of the dot leads to longer lifetimes (hence the smaller oscillator strengths) [33]. This can be related to a decreasing overlap between the electron and hole wave functions. On the other hand, the lifetime dependence on the QD material composition is nonmonotonic. In the regime of low In content, the lifetime decreases, which can be again attributed to changes in the electron-hole wave function overlap. However, the further increase of the In content results in longer lifetimes. This behavior is mainly because the interband momentum matrix element is smaller in InAs than in GaAs.

We show the results for the CI containing 12 electron and 12 hole states [Figs. 4(b) and 4(d)] and the ones from the Hartree approximation (which corresponds to the CI basis truncated to 2 states) [Figs. 4(a) and 4(c)]. As expected [84], the correlations strongly enhance the oscillator strength; hence, the lifetime is reduced.

We compared the tight-binding results for two cases. In the first one, the oscillator strength is obtained using the position operator [Eq. (13)]. In the second one, it is calculated from the momentum matrix elements [Eq. (15)] via the Hellmann-Feynman theorem [Eq. (16)]. Although these models are very different, the results are in good agreement, with a few percent of difference. Here, the lifetimes obtained from the Hellmann-Feynman theorem are systematically shorter.

Finally, we compared the tight-binding and the $k\cdot p$ results. While the obtained dependencies are consistent qualitatively, the discrepancy is considerably larger. Here, the lifetimes coming from the $k\cdot p$ model are systematically smaller, up to about 30% for high In contents.

D. Overhauser field

The coupling between the carriers and the nuclear spins can be studied in terms of the fluctuations of the Overhauser field. We consider the longitudinal and the transverse components of this field (with respect to the growth axis) in terms of the root-mean-square (rms) averages: $\langle h_z^2\rangle^{1/2}$ and

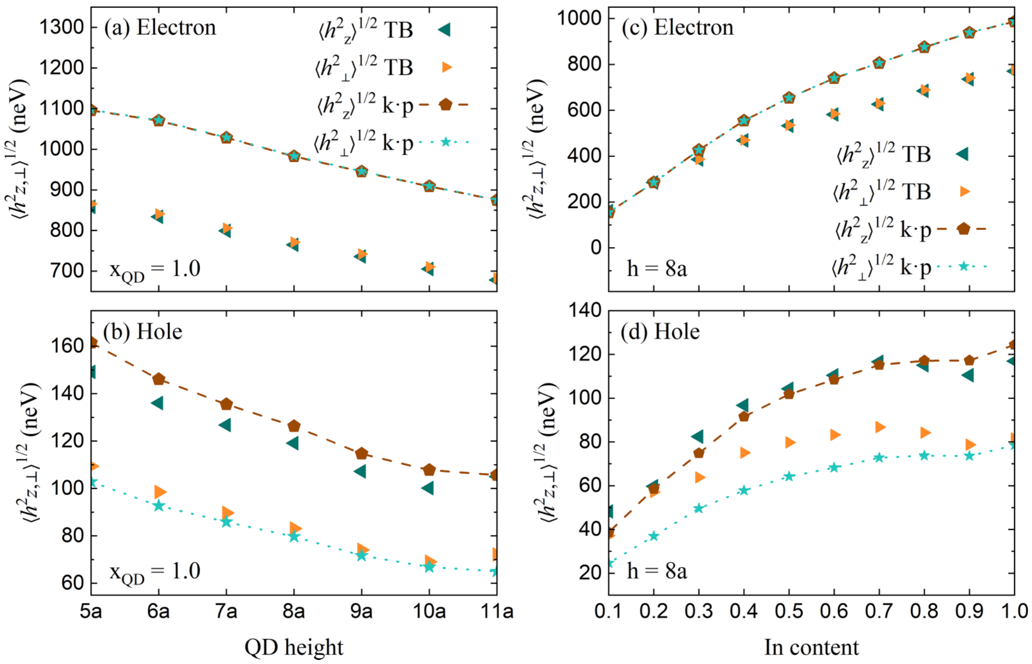

FIG. 5. The fluctuations of the longitudinal and the transverse Overhauser field components calculated for the ground Zeeman doublet, for electron and hole, the dependence on the QD height [(a) and (b)] and the QD composition [(c) and (d)]. For the height dependence [(a) and (b)], the QD composition is fixed to $x_{\mathrm{QD}} = 1.0$. In the composition dependence [(c) and (d)], the height is fixed to $h = 8a$.

$\langle h_\perp^2\rangle^{1/2} = \langle (h_x^2 + h_y^2)/2\rangle^{1/2}$, respectively. As in the previous calculations, we assume the magnetic field $B = 0.1$ T along the growth direction.

The results for the electron are shown in Figs. 5(a) and 5(c). Owing to the dominant s-type orbital composition of the electron states, the field is highly isotropic (i.e. $\langle h_z^2\rangle \approx \langle h_\perp^2\rangle$). In Fig. 5(a), the rms of the Overhauser field components are calculated as a function of the QD height (while the other parameters are kept constant). The values are decreasing, which is attributed to the increasing volume of the QD (with an approximate scaling $\propto 1/\sqrt{V}$), hence the increasing participation number [40,85]. As demonstrated in Fig. 5(c), the rms of the Overhauser field fluctuations strongly increases with the increasing In content. This is attributed to larger nuclear magnetic moments of In atoms (as compared to Ga) and the decreasing wave function participation number, which is due to stronger confinement [40].

The Overhauser field for a hole is presented in Figs. 5(b) and 5(d). The values are several times smaller as compared to the electron ones. This is expected behavior, as the hole wave function is composed mainly of the p- and d-type orbitals, which have zeros at the nuclei. This, in turn, leads to the vanishing of the contact term in the hyperfine interaction Hamiltonian. In contrast to the electron case, there is considerable anisotropy between the longitudinal and the transverse field components. The latter is strongly enhanced by the d-type admixtures in the wave function [40,41].

The results obtained from the $k\cdot p$ and tight-binding models agree reasonably well, especially for holes. However, there is a systematic difference of about 200 neV in the results for electron in the dependence on the QD height [Fig. 5(a)]. This holds at high In concentrations [see Fig. 5(c)], but vanishes for the In content $x_{\mathrm{QD}} < 0.5$. This behavior is attributed to the larger spread of the electron wave function predicted by the TB than by the $k\cdot p$ model. As can be seen in Figs. 5(b) and 5(d), the agreement for the holes is generally better.

VIII. CONCLUSIONS

We have presented a comprehensive comparative analysis of two major theoretical frameworks—atomistic $sp^3d^5s^*$ tight-binding and continuum eight-band $k\cdot p$ models—for describing the spin and optical properties of InGaAs/GaAs quantum dots. Our study spans critical physical observables including single-particle energy levels, g factors for electrons and holes, radiative exciton lifetimes, and the Overhauser field fluctuations arising from hyperfine interactions.

The tight-binding model, with its atomistic resolution, naturally incorporates strain, atomic-scale interface, and material heterogeneity, i.e., alloying. On the other hand, the eight-band $k\cdot p$ approach is more computationally efficient and relies directly on empirical quantities (like the band gap, effective masses, etc.). While both models predict qualitatively consistent trends, we find notable quantitative differences attributable to their intrinsic methodological assumptions.

We introduce and validate several improvements to the $k\cdot p$ framework, including second-order deformation potentials, modified remote-band corrections for g-factor modeling, and an effective grid-scaling scheme. These refinements significantly improve the agreement with tight-binding results, particularly for the electron g factors and single-particle energies. For hole states, discrepancies are more persistent, likely due to their stronger sensitivity to shear strain and complex band mixing effects.

For exciton lifetimes, we demonstrate that both tight-binding and $k\cdot p$ models produce consistent trends with dot size and composition, though differences of up to 30% can occur, especially at high indium concentrations, which is, however, relatively small taking into account substantial methodological differences and also notable dispersion of lifetimes reported experimentally [86]. The tight-binding model shows strong internal consistency across alternative schemes for oscillator strength calculation, reinforcing its robustness.

Importantly, our comparison of hyperfine-induced Overhauser fields confirms that the eight-band $k\cdot p$ method—despite its continuous nature—can approximate atomistic spin decoherence mechanisms with reasonable accuracy, provided appropriate modeling of Bloch functions and orbital character is adopted.

ACKNOWLEDGMENTS

K.G. acknowledges the financing of the MEEDGARD project funded within the QuantERA II Program that has received funding from the European Union's Horizon 2020 research and innovation program under Grant Agreement No. 101017733 and National Centre for Research and Development, Poland—project No. QUANTERAII/2/56/MEEDGARD/2024. Created using resources provided by Wroclaw Centre for Networking and Supercomputing.

DATA AVAILABILITY

The data that support the findings of this study are available as Supplemental Material. Other data may be available from the authors upon reasonable request

APPENDIX: CALCULATION DETAILS

1. Strain

In Martin's formulation of the Valence Force Field (VFF) model, the elastic energy takes the form [43,44]

$$U_{\mathrm{M}} = \sum_{i}\sum_{j}^{\mathrm{NN}(i)}\Bigg\{\frac{1}{4}k_{ij}^{(\mathrm{r})}(r_{ij}-d_{ij})^2 + \sum_{k\neq i,k>j}\bigg[\frac{1}{2}K_{ijk}^{(\theta)}\,d_{ij}d_{ik}\left(\theta_{ijk}-\theta_{ijk}^{(0)}\right)^2 + K_{ijk}^{(\mathrm{rr})}(r_{ij}-d_{ij})(r_{ik}-d_{ik}) + K_{ijk}^{(\mathrm{r}\theta)}[d_{ij}(r_{ij}-d_{ij})+d_{ik}(r_{ik}-d_{ik})]\left(\theta_{ijk}-\theta_{ijk}^{(0)}\right)\bigg]\Bigg\},$$

where $\mathrm{NN}(i)$ are the nearest neighbors of the ith atom, $r_{ij} = |\boldsymbol{r}_{ij}|$ with $\boldsymbol{r}_{ij} = \boldsymbol{R}_j - \boldsymbol{R}_i$ is the actual distance between the atomic nodes localized at sites $\boldsymbol{R}_i$ and $\boldsymbol{R}_j$, d_{ij} denotes the ideal (for an unstrained bulk crystal) distance between these atoms, which in the zincblende structure is $d = \sqrt{3}a/4$; the actual bond angle is given by

$$\theta_{ijk} = \arccos\left(\frac{\boldsymbol{r}_{ij}\cdot\boldsymbol{r}_{ik}}{r_{ij}r_{ik}}\right),$$

and $\theta_{ijk}^{(0)} = \arccos(-1/3)$ is its ideal (unstrained) value; $k_{ij}^{(\mathrm{r})}$ is the $k^{(\mathrm{r})}$ bulk parameter for the material defined by the pair of atoms i and j. The parameters involving three atoms are calculated by averaging $K_{ijk}^{(\alpha)} = (k_{ij}^{(\alpha)} + k_{ik}^{(\alpha)})/2$ where $\alpha = \{\text{“}\theta\text{”}, \text{“rr”}, \text{“r}\theta\text{”}\}$. These parameters are directly related to the elastic constants (C_{11}, C_{12}, and C_{44}) and the Kleinmann parameter (ζ) by the analytic formulas [44]

$$k^{(\mathrm{r})} = a\left[\frac{C_{11}(2+2\zeta+5\zeta^2)+C_{12}(1-8\zeta-2\zeta^2)}{4(1-\zeta)^2} + \frac{3C_{44}(1-4\zeta)}{4(1-\zeta)^2}\right], \tag{A1a}$$

$$k^{(\theta)} = \frac{a(C_{11}-C_{12})}{6}, \tag{A1b}$$

$$k^{(\mathrm{rr})} = a\left[\frac{C_{11}(2-10\zeta-\zeta^2)+C_{12}(7-8\zeta+10\zeta^2)}{24(1-\zeta)^2} - \frac{3C_{44}(1-4\zeta)}{24(1-\zeta)^2}\right], \tag{A1c}$$

$$k^{(\mathrm{r}\theta)} = a\sqrt{2}\frac{(C_{11}-C_{12})(1+2\zeta)-3C_{44}}{12(\zeta-1)}. \tag{A1d}$$

TABLE I. The material parameters.

	InAs	GaAs
a (Å)	6.0583[a]	5.65325[a]
C_{11} (GPa)	83.3[a]	122.1[a]
C_{12} (GPa)	45.3[a], 45.0[d]	56.6[a]
C_{44} (GPa)	39.6[a], 37.5[d]	60.0[a]
ζ	0.687[b]	0.547[b]
$k^{(\mathrm{r})}$ (eV/Å^2)	3.491[c]	5.229[c]
$k^{(\theta)}$ (eV/Å^2)	0.241[c]	0.385[c]
$k^{(\mathrm{rr})}$ (eV/Å^2)	0.510[c]	0.512[c]
$k^{(\mathrm{r}\theta)}$ (eV/Å^2)	0.307[c]	0.393[c]

[a] Values from Ref. [89].
[b] Values from Ref. [44].
[c] Values calculated from the elastic constants.
[d] The reduced values for Martin's VFF model.

To reproduce Vegard's law for alloy, in the case of the mixed bonds (In–As–Ga and Ga–As–In), the bond angle is set to $\theta_{ijk}^{(0)} = 110.5^\circ$ [23]. Martin's model in its full version (which includes the long-range Coulomb terms) is capable of accounting for all three elastic constants and the Kleinmann parameter simultaneously. However, we utilize the covalent approximation [44,87], where Coulomb terms are neglected. Such an approximation is not valid if the anisotropy factor $A = 2C_{44}/(C_{11}-C_{12})$ is greater than 2 [44], which is the case for InAs. To overcome this problem, we use slightly reduced C_{12} and C_{44}, compared to the literature values (see Table I).

To obtain relaxed atomic positions, we start with the situation where all atoms in the structure are artificially matched to the barrier (GaAs) lattice constant. Then we perform numerical minimization of U_M using the PETSC TAO library [88].

2. Tight-binding model

The tight-binding Hamiltonian H^{TB} is originally written in the real basis [47] of $s, p_x, p_y, p_z, d_{xy}, d_{yz}, d_{zx}, d_{x^2-y^2}, d_{3z^2-r^2}, s^*$

orbitals with two spin configurations. In this basis, the orbital angular momentum on-site matrices (for a given spin) take the form

$$L_x = i\hbar\begin{pmatrix} 0 & 0 & 0 & 0 & 0 & 0 & 0 & 0 & 0 & 0\\ 0 & 0 & 0 & 0 & 0 & 0 & 0 & 0 & 0 & 0\\ 0 & 0 & 0 & -1 & 0 & 0 & 0 & 0 & 0 & 0\\ 0 & 0 & 1 & 0 & 0 & 0 & 0 & 0 & 0 & 0\\ 0 & 0 & 0 & 0 & 0 & 0 & -1 & 0 & 0 & 0\\ 0 & 0 & 0 & 0 & 0 & 0 & 0 & -1 & -\sqrt{3} & 0\\ 0 & 0 & 0 & 0 & 1 & 0 & 0 & 0 & 0 & 0\\ 0 & 0 & 0 & 0 & 0 & 1 & 0 & 0 & 0 & 0\\ 0 & 0 & 0 & 0 & 0 & \sqrt{3} & 0 & 0 & 0 & 0\\ 0 & 0 & 0 & 0 & 0 & 0 & 0 & 0 & 0 & 0 \end{pmatrix}, \tag{A2}$$

$$L_y = i\hbar\begin{pmatrix} 0 & 0 & 0 & 0 & 0 & 0 & 0 & 0 & 0 & 0\\ 0 & 0 & 0 & 1 & 0 & 0 & 0 & 0 & 0 & 0\\ 0 & 0 & 0 & 0 & 0 & 0 & 0 & 0 & 0 & 0\\ 0 & -1 & 0 & 0 & 0 & 0 & 0 & 0 & 0 & 0\\ 0 & 0 & 0 & 0 & 0 & 1 & 0 & 0 & 0 & 0\\ 0 & 0 & 0 & 0 & -1 & 0 & 0 & 0 & 0 & 0\\ 0 & 0 & 0 & 0 & 0 & 0 & 0 & -1 & \sqrt{3} & 0\\ 0 & 0 & 0 & 0 & 0 & 0 & 1 & 0 & 0 & 0\\ 0 & 0 & 0 & 0 & 0 & 0 & -\sqrt{3} & 0 & 0 & 0\\ 0 & 0 & 0 & 0 & 0 & 0 & 0 & 0 & 0 & 0 \end{pmatrix}, \tag{A3}$$

$$L_z = i\hbar\begin{pmatrix} 0 & 0 & 0 & 0 & 0 & 0 & 0 & 0 & 0 & 0\\ 0 & 0 & -1 & 0 & 0 & 0 & 0 & 0 & 0 & 0\\ 0 & 1 & 0 & 0 & 0 & 0 & 0 & 0 & 0 & 0\\ 0 & 0 & 0 & 0 & 0 & 0 & 0 & 0 & 0 & 0\\ 0 & 0 & 0 & 0 & 0 & 0 & 0 & 2 & 0 & 0\\ 0 & 0 & 0 & 0 & 0 & 0 & 1 & 0 & 0 & 0\\ 0 & 0 & 0 & 0 & 0 & -1 & 0 & 0 & 0 & 0\\ 0 & 0 & 0 & 0 & -2 & 0 & 0 & 0 & 0 & 0\\ 0 & 0 & 0 & 0 & 0 & 0 & 0 & 0 & 0 & 0\\ 0 & 0 & 0 & 0 & 0 & 0 & 0 & 0 & 0 & 0 \end{pmatrix}, \tag{A4}$$

where, for clarity, the subspace related to the p shell (d shell) is marked by the red (blue) color. One should note that the tight-binding orbitals have s, p, and d character under the crystal symmetry operations (not under the full rotational group). Therefore the presented L_i matrices are a kind of approximation.

To transform the Hamiltonian from the basis $\mathcal{B} = \{s, p_x, p_y, p_z, d_{xy}, d_{yz}, d_{zx}, d_{x^2-y^2}, d_{3z^2-r^2}, s^*\}$ to the orbital angular momentum basis $\mathcal{B}' = \{s, p_{-1}, p_0, p_1, d_{-2}, d_{-1}, d_0, d_1, d_2, s^*\}$, we used the transformation

$$H^{(\mathrm{TB})'} = \mathcal{P}^{\dagger} H^{(\mathrm{TB})} \mathcal{P}, \tag{A5}$$

where

$$\mathcal{P} = \begin{pmatrix} \mathcal{P}_{\mathrm{orb}} & 0\\ 0 & \mathcal{P}_{\mathrm{orb}} \end{pmatrix}, \tag{A6}$$

with

$$\mathcal{P}_{\mathrm{orb}} = \begin{pmatrix} 1 & 0 & 0 & 0 & 0 & 0 & 0 & 0 & 0 & 0\\ 0 & \frac{1}{\sqrt{2}} & 0 & -\frac{1}{\sqrt{2}} & 0 & 0 & 0 & 0 & 0 & 0\\ 0 & -\frac{i}{\sqrt{2}} & 0 & -\frac{i}{\sqrt{2}} & 0 & 0 & 0 & 0 & 0 & 0\\ 0 & 0 & 1 & 0 & 0 & 0 & 0 & 0 & 0 & 0\\ 0 & 0 & 0 & 0 & -\frac{i}{\sqrt{2}} & 0 & 0 & 0 & \frac{i}{\sqrt{2}} & 0\\ 0 & 0 & 0 & 0 & 0 & -\frac{i}{\sqrt{2}} & 0 & -\frac{i}{\sqrt{2}} & 0 & 0\\ 0 & 0 & 0 & 0 & 0 & \frac{1}{\sqrt{2}} & 0 & -\frac{1}{\sqrt{2}} & 0 & 0\\ 0 & 0 & 0 & 0 & \frac{1}{\sqrt{2}} & 0 & 0 & 0 & \frac{1}{\sqrt{2}} & 0\\ 0 & 0 & 0 & 0 & 0 & 0 & 1 & 0 & 0 & 0\\ 0 & 0 & 0 & 0 & 0 & 0 & 0 & 0 & 0 & 1 \end{pmatrix}.$$

All subsequent calculations are performed in the $\mathcal{B}'$ basis.

3. Eight-band $\boldsymbol{k}\cdot\boldsymbol{p}$

The electron effective mass m_{e}^* is extracted from the tight-binding model band structures by calculating numerically second derivative

$$\frac{1}{m_{\mathrm{e}}^*} = \frac{1}{\hbar^2}\frac{\partial^2 E^{(\mathrm{c})}}{\partial k_z^2}\bigg|_{k_z=0}.$$

Here, the k_z component is arbitrarily chosen, due to the isotropic character of the conduction band effective mass. To obtain the Luttinger parameters, we first calculate the VB effective masses in the [001] and [111] directions. To lift the heavy- and light-hole band degeneracy, we applied vanishing biaxial strain. Then, we use the formulas [89]

$$\gamma_1 = \frac{1}{2}\left(\frac{m_0}{m_{\mathrm{lh},001}^*} + \frac{m_0}{m_{\mathrm{hh},001}^*}\right),$$

$$\gamma_2 = \frac{1}{4}\left(\frac{m_0}{m_{\mathrm{lh},001}^*} - \frac{m_0}{m_{\mathrm{hh},001}^*}\right),$$

$$\gamma_3 = \frac{1}{4}\left(\frac{m_0}{m_{\mathrm{lh},111}^*} - \frac{m_0}{m_{\mathrm{hh},111}^*}\right).$$

The deformation potentials were extracted by fitting to the TB band edges with the second-order strain scheme [62,81].

To avoid spurious solutions [59] related to the losing ellipticity of the $k\cdot p$ Hamiltonian, the E_{P} is reduced according the the formula [90]

$$E_{\mathrm{P}}^{(\mathrm{red})} = \left(\frac{m_0}{m_{\mathrm{e}}^*} - 1\right)\frac{E_{\mathrm{g}}(E_{\mathrm{g}} + \Delta_0)}{E_{\mathrm{g}} + 2\Delta_0/3},$$

which gives $A' = 1$

The bulk g factors for: the electron (g), the heavy-hole (g_{hh}), and the light-hole (g_{lh}) are calculated from the TB within the linear response theory [9,56]. Then, using the relations (in the electron picture) [57]

$$g_{hh} = 6\kappa + \tfrac{27}{2}q,$$

$$g_{lh} = 2\kappa + \tfrac{1}{2}q,$$

we extracted κ and q.

The obtained values are shown in Table. II and listed in Ref. [100]. The table also contains a comparison to the parameters recommended by Vurgaftman *et al.* [89]. In most cases,

TABLE II. Band structure parameters used in the $k\cdot p$ calculations and the literature values (in most cases, the ones recommended by Vurgaftman [89]).

	This work		Literature values	
	GaAs	InAs	GaAs	InAs
E_g (eV)	1.519	0.418	1.519 [91]	0.417 [92]
E_p(eV)	25.31	21.06	28.8 [93], 25.0 [94]	21.5 [95]
$E_p^{(red)}$(eV)	22.56	20.62	–	–
Δ_0(eV)	0.340	0.380	0.341 [96]	0.39 [89]
m_e^* (m_0)	0.0669	0.0235	0.067 [97]	0.026 [89]
γ_1	7.35	18.85	6.98 [89]	20.0 [89]
γ_2	2.14	7.86	2.06 [89]	8.5 [89]
γ_3	3.13	8.90	2.93 [89]	9.2 [89]
g	−0.066	−14.18	−0.44 [57]	−14.9 [57]
κ	1.53	7.18	1.2 [57]	7.6 [57]
q	0.03	0.08	0.04 [98]	0.04 [98]
a_c	−6.79 [81]	−4.78 [81]	−7.17[d]	−5.08[d]
a_v	1.88 [81]	1.26 [81]	−1.16[d]	−1.0[d]
b_v	−1.84 [81]	−1.76 [81]	−2.0[d]	−1.8[d]
d_v	−2.54 [81]	−3.33 [81]	−4.8[d]	−3.6[d]

[a] Reference [91].

[b] Reference [94].

[c] Reference [93].

[d] Deformation potentials from Ref. [99]. Note the different sign convention in a_v.

the agreement is satisfactory, yet the highest discrepancies are visible for GaAs deformation potentials.

As demonstrated in Fig. 6, we get a very good agreement between the $k\cdot p$ and the TB bulk band structures in the vicinity of the Γ point in the BZ. The strongest confinement in a lens-shaped QD is in the z direction. The QD height $h = 6a$ (the smallest considered one) can be roughly connected to the characteristic wavevector $k_z = \frac{\pi}{6a}$, which is 1/12 of the path between the Γ and X point. In this range, the difference between the $k\cdot p$ and TB band structures is on the order of a few meV.

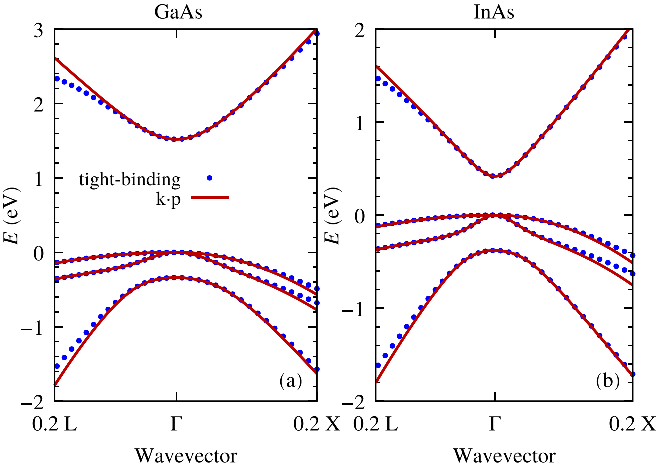

FIG. 6. The band structures for InAs and GaAs calculated using the eight-band $k\cdot p$ and $sp^3d^5s^*$ TB. Here “0.2L ” and “0.2 X” means 20% of the path from Γ to the X and L point, respectively.

The values of the reduced Luttinger parameters γ'_{1-3} are calculated from [57]

$$\gamma'_1 = \gamma_1 - \frac{1}{3}\frac{E_P^{(red)}}{E_g},$$

$$\gamma'_2 = \gamma_2 - \frac{1}{6}\frac{E_P^{(red)}}{E_g},$$

$$\gamma'_3 = \gamma_3 - \frac{1}{6}\frac{E_P^{(red)}}{E_g}.$$

4. Coulomb matrix elements and lifetime calculations

The electron-hole direct Coulomb matrix elements are defined by

$$V_{ijj'i'} = \frac{|e|^2}{4\pi\epsilon_0\epsilon_r}\int d\boldsymbol{r}\int d\boldsymbol{r}'\,\frac{\psi_i^{(e)*}(\boldsymbol{r})\psi_j^{(h)*}(\boldsymbol{r}')\psi_{j'}^{(h)}(\boldsymbol{r}')\psi_{i'}^{(e)}(\boldsymbol{r})}{|\boldsymbol{r}-\boldsymbol{r}'|},$$

where $\psi_i^{(e)}(\boldsymbol{r})$ and $\psi_i^{(h)}(\boldsymbol{r})$ are electron and hole wave functions, respectively; ϵ_r is the relative permittivity (we took $\epsilon_r = 12.4$ which is the value for GaAs [57]). The calculations can be optimized by moving to the reciprocal space. In view of the Fourier theorem

$$\frac{1}{|\boldsymbol{r}-\boldsymbol{r}'|} = \frac{1}{(2\pi)^3}\int \frac{4\pi}{q^2}e^{i\boldsymbol{q}(\boldsymbol{r}-\boldsymbol{r}')}d\boldsymbol{q},$$

which gives

$$V_{ijj'i'} = \frac{|e|^2}{8\pi^3\epsilon_0\epsilon_r}\int \mathcal{F}_{ii'}^{(e)}(\boldsymbol{q})\mathcal{F}_{j'j}^{(h)*}(\boldsymbol{q})\frac{1}{q^2}d\boldsymbol{q},$$

where $\mathcal{F}_{ij}(\boldsymbol{q})$ are the form-factors given by

$$\mathcal{F}_{ij}(\boldsymbol{q}) = \int \psi_i^*(\boldsymbol{r})\psi_j(\boldsymbol{r})e^{i\boldsymbol{q}\boldsymbol{r}}d\boldsymbol{r}.$$

For the eight-band $k\cdot p$ model (within the envelope function approximation), the wave functions are represented by

$$\psi_n(\boldsymbol{r}) = \sum_{m=1}^{8} F_m^{(n)}(\boldsymbol{r})\,u_m(\boldsymbol{r}),$$

where $u_m(\boldsymbol{r})$ are the Bloch functions at the band edge $\boldsymbol{k} = 0$, while $F_m^{(n)}(\boldsymbol{r})$ is a subband-dependent envelope. In this model, the form-factors are calculated by

$$\mathcal{F}_{ij}(\boldsymbol{q}) \approx \sum_{m=1}^{8}\int F_m^{(i)*}(\boldsymbol{r})F_m^{(j)}(\boldsymbol{r})e^{i\boldsymbol{q}\boldsymbol{r}}d\boldsymbol{r},$$

where we assumed that $e^{i\boldsymbol{q}\boldsymbol{r}}$ changes slowly in the length of the unit cell, hence $\langle u_m|e^{i\boldsymbol{q}\boldsymbol{r}}|u_{m'}\rangle \approx \delta_{mm'}$. We calculated $\mathcal{F}_{ij}(\boldsymbol{q})$ using the FFTW library [101] with the wave functions represented on the Cartesian grid.

In the case of the tight-binding model, we calculated the Coulomb matrix elements, neglecting the short-range (hence basis-dependent) interaction terms. We also performed the calculations in the reciprocal space. However, owing to the underlying atomic lattice, which does not match the cartesian grid, the form-factors were obtained using the nonuniform fast Fourier transform with the FINUFFT library [102–104]. The model is described in detail in Appendix of Ref. [32].

The frequency-dependent refractive index in the radiative lifetime calculations was taken from the wavelength-dependent one $n(\omega) = \tilde{n}(2\pi c/\omega)$, that is defined by the Sellmeier-like parameters

$$\tilde{n}(\lambda) = \sqrt{A + \frac{B\lambda^2}{\lambda^2 - C^2} + \frac{D\lambda^2}{\lambda^2 - E^2}},$$

where for GaAs: $A = 3.5$, $B = 7.4969$, $C = 0.4082$ µm, $D = 1.9347$, and $E = 37.17$ µm [79].

5. Hyperfine interaction

To obtain the fluctuations of the Overhauser field $\langle h_j^2\rangle$ [Eq. (17)] for the electron or hole doublet $\{|\psi_1\rangle, |\psi_2\rangle\}$, one needs to calculate

$$\mathrm{Tr}\{A_i(\boldsymbol{r} - \boldsymbol{R}_n)\widetilde{\sigma}_j\} = \sum_{\lambda=1}^{2}\langle\psi_\lambda|A_i(\boldsymbol{r} - \boldsymbol{R}_n)\widetilde{\sigma}_j|\psi_\lambda\rangle,$$

where

$$\begin{aligned}\widetilde{\sigma}_x &= |\psi_1\rangle\langle\psi_2| + |\psi_2\rangle\langle\psi_1|,\\ \widetilde{\sigma}_y &= -i|\psi_1\rangle\langle\psi_2| + i|\psi_2\rangle\langle\psi_1|,\\ \widetilde{\sigma}_z &= |\psi_1\rangle\langle\psi_1| - |\psi_2\rangle\langle\psi_2|.\end{aligned}$$

The matrix elements $A_{i,\lambda\lambda'} = \langle\psi_\lambda|A_i(\boldsymbol{r} - \boldsymbol{R}_n)|\psi_{\lambda'}\rangle$ were calculated from

$$\begin{aligned}A_{i,\lambda\lambda'} &= \sum_{n',n''}\sum_{\alpha,\alpha'} w^{(\lambda)*}_{n',\alpha} w^{(\lambda')}_{n'',\alpha'}\langle\boldsymbol{R}_{n'};\alpha|A_i(\boldsymbol{r} - \boldsymbol{R}_n)|\boldsymbol{R}_{n''};\alpha'\rangle\\ &\approx \sum_{\alpha,\alpha'} w^{(\lambda)*}_{n,\alpha} w^{(\lambda')}_{n,\alpha'}\langle\boldsymbol{R}_n;\alpha|A_i(\boldsymbol{r} - \boldsymbol{R}_n)|\boldsymbol{R}_n;\alpha'\rangle,\end{aligned}$$

where we neglected the terms involving different atomic sites. As the last matrix element does not depend on the atomic position, we simplify the notation to

$$\langle\boldsymbol{R}_n;\alpha|A_i(\boldsymbol{r} - \boldsymbol{R}_n)|\boldsymbol{R}_n;\alpha'\rangle \equiv \langle\alpha|A_i(\boldsymbol{r})|\alpha'\rangle.$$

To calculate these terms, the TB orbitals were represented by the functions

$$\langle\boldsymbol{r}|\alpha\rangle = \varphi_\alpha(\boldsymbol{r})|s_\alpha\rangle,$$

where $s_\alpha \equiv s = \pm\frac{1}{2}$ denotes the spin, and owing to the symmetry

$$\varphi_\alpha(\boldsymbol{r}) = \mathcal{R}_\alpha(r)Y_m^l(\theta, \phi)$$

where $\mathcal{R}_\alpha(r)$ is the radial part of the orbital, l is the azimuthal number, and m is the magnetic quantum number, both corresponding to a given α. Due to the involved spherical symmetry, it is beneficial to represent $\boldsymbol{A}$ in terms of the spherical vector components

$$\begin{aligned}A_x &= \frac{\mathcal{A}^{(1)}_{-1} - \mathcal{A}^{(1)}_{+1}}{\sqrt{2}},\\ A_y &= i\frac{\mathcal{A}^{(1)}_{-1} + \mathcal{A}^{(1)}_{+1}}{\sqrt{2}},\\ A_z &= \mathcal{A}^{(1)}_0,\end{aligned}$$

where the number in the bracket denotes the tensor rank. The matrix elements of $\mathcal{A}^{(1)}_q$ between the orbital states are [40]

$$\begin{aligned}\langle\alpha|\mathcal{A}^{(1)}_q|\alpha'\rangle = \frac{\mu_0\mu_B}{2\pi\hbar}\bigg[&\frac{2}{3}\mathcal{R}^*_\alpha(0)\mathcal{R}_{\alpha'}(0)\left\langle\frac{1}{2}s\middle|S^{(1)}_q\middle|\frac{1}{2}s'\right\rangle\delta_{l0}\,\delta_{l'0}\\ &+ \widetilde{M}_{ll}\langle lm|L^{(1)}_q|lm'\rangle\delta_{ll'}\delta_{ss'}\\ &- \sqrt{8\pi}\widetilde{M}_{ll'}\sum_{q_1,q_2}\langle 2, 1; q_1, q_2|2, 1; 1, q\rangle\\ &\times G^{mq_1m'}_{l2l'}\left\langle\frac{1}{2}s\middle|S^{(1)}_{q_2}\middle|\frac{1}{2}s'\right\rangle\bigg],\end{aligned} \tag{A7}$$

where

$$\widetilde{M}_{ll'} = \int r^2\mathcal{R}^*_\alpha(r)\frac{1}{r^3}\mathcal{R}_{\alpha'}(r)dr,$$

$G^{mm'm''}_{ll'l''}$ are the Gaunt coefficients. From the Wigner-Eckart theorem

$$\left\langle\frac{1}{2}s\middle|S^{(1)}_q\middle|\frac{1}{2}s'\right\rangle = \frac{\sqrt{3}\hbar}{2}\left\langle\frac{1}{2}, 1; s', q\middle|\frac{1}{2}, 1; \frac{1}{2}, s\right\rangle, \quad \langle lm|L^{(1)}_q|lm'\rangle = \hbar\sqrt{l(l+1)}\langle l, 1; m', q|l, 1; l, m\rangle.$$

The three terms in the bracket in Eq. (A7) are the contact part, the orbital part, and the dipolar part, respectively. The contact part is nonzero only for *s*-type orbitals, as the others vanish at r = 0. If we approximate the TB orbital $\mathcal{R}_{S^*}(r)$ by $\mathcal{R}_S(r)$, one can write

$$\begin{aligned}\langle\alpha|\mathcal{A}^{(1)}_q|\alpha'\rangle = \frac{\mu_0\mu_B}{2\pi\hbar}|\mathcal{R}_S(0)|^2\bigg[&\frac{2}{3}\left\langle\frac{1}{2}s\middle|S^{(1)}_q\middle|\frac{1}{2}s'\right\rangle\delta_{l0}\,\delta_{l'0} + M_{ll}\langle lm|L^{(1)}_q|lm'\rangle\delta_{ll'}\delta_{ss'}\\ &- \sqrt{8\pi}M_{ll'}\sum_{q_1,q_2}\langle 2, 1; q_1, q_2|2, 1; 1, q\rangle G^{mq_1m'}_{l2l'}\left\langle\frac{1}{2}s\middle|S^{(1)}_{q_2}\middle|\frac{1}{2}s'\right\rangle\bigg],\end{aligned}$$

where $M_{ll'} = \widetilde{M}_{ll'}/|\mathcal{R}_S(0)|^2$.

Finally, the tight-binding basis was represented by hydrogen-like orbitals [$\mathcal{R}_\alpha(r) \to \mathcal{R}_{nl}(r)$]

$$\mathcal{R}_{nl}(r) = \sqrt{\frac{(2\xi)^3(n-l-1)!}{2n(n+l)!\,a_\mathrm{B}^3}}\left(\frac{2\xi r}{a_\mathrm{B}}\right)^l \exp\left(-\frac{\xi r}{a_\mathrm{B}}\right) L_{n-l-1}^{2l+1}\left(\frac{2\xi r}{a_\mathrm{B}}\right),$$

where $L_{n-l-1}^{2l+1}(x)$ are the generalized Laguerre polynomials. Therefore $\mathcal{R}_S(0) = 2\sqrt{(\xi_S/a_\mathrm{B})^3}$. In the case of Ga and As, we took the orbitals: $4s$, $4p$, $3d$; and for In: $5s$, $5p$, $4d$ [40,41]. The values of ξ_S, ξ_P, ξ_D exponents and $M_{ll'}$ for the relevant atoms, are given in Ref. [40].

[1] M. Reindl, J. H. Weber, D. Huber, C. Schimpf, S. F. Covre da Silva, S. L. Portalupi, R. Trotta, P. Michler, and A. Rastelli, Highly indistinguishable single photons from incoherently excited quantum dots, Phys. Rev. B **100**, 155420 (2019).

[2] P. Lodahl, Quantum-dot based photonic quantum networks, Quantum Sci. Technol. **3**, 013001 (2018).

[3] C. Shang, M. De Gregorio, Q. Buchinger, M. Meinecke, P. Gschwandtner, A. Pfenning, T. Huber-Loyola, S. Hoefling, and J. E. Bowers, Ultra-low density and high performance InAs quantum dot single photon emitters, APL Quantum **1**, 036115 (2024).

[4] S. E. Economou, N. Lindner, and T. Rudolph, Optically generated 2-dimensional photonic cluster state from coupled quantum dots, Phys. Rev. Lett. **105**, 093601 (2010).

[5] H. Kosaka, D. S. Rao, H. D. Robinson, P. Bandaru, K. Makita, and E. Yablonovitch, Single photoelectron trapping, storage, and detection in a field effect transistor, Phys. Rev. B **67**, 045104 (2003).

[6] R. Vrijen and E. Yablonovitch, A spin-coherent semiconductor photo-detector for quantum communication, Phys. E **10**, 569 (2001).

[7] M. Gawełczyk, M. Krzykowski, K. Gawarecki, and P. Machnikowski, Controllable electron spin dephasing due to phonon state distinguishability in a coupled quantum dot system, Phys. Rev. B **98**, 075403 (2018).

[8] L. M. Roth, B. Lax, and S. Zwerdling, Theory of optical magneto-absorption effects in semiconductors, Phys. Rev. **114**, 90 (1959).

[9] A. A. Kiselev, E. L. Ivchenko, and U. Rössler, Electron g factor in one- and zero-dimensional semiconductor nanostructures, Phys. Rev. B **58**, 16353 (1998).

[10] G. Medeiros-Ribeiro, E. Ribeiro, and H. Westfahl, Jr., g factor engineering and control in self-assembled quantum dots, Appl. Phys. A **77**, 725 (2003).

[11] T. Nakaoka, T. Saito, J. Tatebayashi, and Y. Arakawa, Size, shape, and strain dependence of the g factor in self-assembled In(Ga)As quantum dots, Phys. Rev. B **70**, 235337 (2004).

[12] K. Gawarecki, Spin-orbit coupling and magnetic-field dependence of carrier states in a self-assembled quantum dot, Phys. Rev. B **97**, 235408 (2018).

[13] M. Bayer, A. Kuther, A. Forchel, A. Gorbunov, V. B. Timofeev, F. Schäfer, J. P. Reithmaier, T. L. Reinecke, and S. N. Walck, Electron and hole g factors and exchange interaction from studies of the exciton fine structure in $\mathrm{In_{0.60}Ga_{0.40}As}$ quantum dots, Phys. Rev. Lett. **82**, 1748 (1999).

[14] G. Medeiros-Ribeiro, M. V. B. Pinheiro, V. L. Pimentel, and E. Marega, Spin splitting of the electron ground states of InAs quantum dots, Appl. Phys. Lett. **80**, 4229 (2002).

[15] N. A. J. M. Kleemans, J. van Bree, M. Bozkurt, P. J. van Veldhoven, P. A. Nouwens, R. Nötzel, A. Y. Silov, P. M. Koenraad, and M. E. Flatté, Size-dependent exciton g factor in self-assembled InAs/InP quantum dots, Phys. Rev. B **79**, 045311 (2009).

[16] A. Schwan, B. M. Meiners, A. Greilich, D. R. Yakovlev, M. Bayer, A. D. Maia, A. A. Quivy, and A. B. Henriques, Anisotropy of electron and hole g factors in (In,Ga)As quantum dots, Appl. Phys. Lett. **99**, 221914 (2011).

[17] T. Nakaoka, T. Saito, J. Tatebayashi, S. Hirose, T. Usuki, N. Yokoyama, and Y. Arakawa, Tuning of g-factor in self-assembled (In,Ga)As quantum dots through strain engineering, Phys. Rev. B **71**, 205301 (2005).

[18] V. Jovanov, T. Eissfeller, S. Kapfinger, E. C. Clark, F. Klotz, M. Bichler, J. G. Keizer, P. M. Koenraad, M. S. Brandt, G. Abstreiter, and J. J. Finley, Highly nonlinear excitonic Zeeman spin splitting in composition-engineered artificial atoms, Phys. Rev. B **85**, 165433 (2012).

[19] T. Andlauer and P. Vogl, Electrically controllable g tensors in quantum dot molecules, Phys. Rev. B **79**, 045307 (2009).

[20] K. Gawarecki and P. Machnikowski, Phonon-assisted relaxation between triplet and singlet states in a self-assembled double quantum dot, Sci. Rep. **11**, 15256 (2021).

[21] W. Sheng and A. Babinski, Zero g factors and nonzero orbital momenta in self-assembled quantum dots, Phys. Rev. B **75**, 033316 (2007).

[22] W. Sheng, S. J. Xu, and P. Hawrylak, Electron g -factor distribution in self-assembled quantum dots, Phys. Rev. B **77**, 241307(R)(2008).

[23] A. J. Williamson, L. W. Wang, and A. Zunger, Theoretical interpretation of the experimental electronic structure of lens-shaped self-assembled InAs/GaAs quantum dots, Phys. Rev. B **62**, 12963 (2000).

[24] M. Bayer, G. Ortner, O. Stern, A. Kuther, A. A. Gorbunov, A. Forchel, P. Hawrylak, S. Fafard, K. Hinzer, T. L. Reinecke, S. N. Walck, J. P. Reithmaier, F. Klopf, and F. Schäfer, Fine structure of neutral and charged excitons in self-assembled In(Ga)As/(Al)GaAs quantum dots, Phys. Rev. B **65**, 195315 (2002).

[25] P. Michler, Single quantum dots: Fundamentals, applications, and new concepts, in *Topics in Applied Physics* (Berlin, Heidelberg, 2003), Vol. 90.

[26] S. Rodt, R. Heitz, A. Schliwa, R. L. Sellin, F. Guffarth, and D. Bimberg, Repulsive exciton-exciton interaction in quantum dots, Phys. Rev. B **68**, 035331 (2003).

[27] A. Schliwa, M. Winkelnkemper, and D. Bimberg, Impact of size, shape, and composition on piezoelectric effects and electronic properties of In(Ga)As/GaAs quantum dots, Phys. Rev. B **76**, 205324 (2007).

[28] O. Stier, M. Grundmann, and D. Bimberg, Electronic and optical properties of strained quantum dots modeled by 8-band $k \cdot p$ theory, Phys. Rev. B **59**, 5688 (1999).

[29] G. W. Bryant and W. Jaskólski, Tight-binding theory of quantum-dot quantum wells: Single-particle effects and near-band-edge structure, Phys. Rev. B **67**, 205320 (2003).

[30] S. Schulz, S. Schumacher, and G. Czycholl, Tight-binding model for semiconductor quantum dots with a wurtzite crystal structure: From one-particle properties to Coulomb correlations and optical spectra, Phys. Rev. B **73**, 245327 (2006).

[31] M. Zieliński, M. Korkusiński, and P. Hawrylak, Atomistic tight-binding theory of multiexciton complexes in a self-assembled InAs quantum dot, Phys. Rev. B **81**, 085301 (2010).

[32] K. Gawarecki, C. Spinnler, L. Zhai, G. N. Nguyen, A. Ludwig, R. J. Warburton, M. C. Löbl, D. E. Reiter, and P. Machnikowski, Symmetry breaking via alloy disorder to explain radiative Auger transitions in self-assembled quantum dots, Phys. Rev. B **108**, 235410 (2023).

[33] S. Stobbe, J. Johansen, P. T. Kristensen, J. M. Hvam, and P. Lodahl, Frequency dependence of the radiative decay rate of excitons in self-assembled quantum dots: Experiment and theory, Phys. Rev. B **80**, 155307 (2009).

[34] M. Gawełczyk, M. Syperek, A. Maryński, P. Mrowiński, Ł. Dusanowski, K. Gawarecki, J. Misiewicz, A. Somers, J. P. Reithmaier, S. Höfling, and G. Sęk, Exciton lifetime and emission polarization dispersion in strongly in-plane asymmetric nanostructures, Phys. Rev. B **96**, 245425 (2017).

[35] M. Lienhart, K. Gawarecki, M. Stöcker, F. Bopp, C. Cullip, N. Akhlaq, C. Thalacker, J. Schall, S. Rodt, A. Ludwig, D. Reuter, S. Reitzenstein, K. Müller, P. Machnikowski, and J. J. Finley, Resonant and anti-resonant exciton-phonon coupling in quantum dot molecules, arXiv:2505.09906 [cond-mat].

[36] J. Fischer, W. A. Coish, D. V. Bulaev, and D. Loss, Spin decoherence of a heavy hole coupled to nuclear spins in a quantum dot, Phys. Rev. B **78**, 155329 (2008).

[37] K. De Greve, P. L. McMahon, D. Press, T. D. Ladd, D. Bisping, C. Schneider, M. Kamp, L. Worschech, S. Höfling, A. Forchel, and Y. Yamamoto, Ultrafast coherent control and suppressed nuclear feedback of a single quantum dot hole qubit, Nature Phys. **7**, 872 (2011).

[38] J. H. Prechtel, A. V. Kuhlmann, J. Houel, A. Ludwig, S. R. Valentin, A. D. Wieck, and R. J. Warburton, Decoupling a hole spin qubit from the nuclear spins, Nat. Mater. **15**, 981 (2016).

[39] B. Urbaszek, X. Marie, T. Amand, O. Krebs, P. Voisin, P. Maletinsky, A. Högele, and A. Imamoglu, Nuclear spin physics in quantum dots: An optical investigation, Rev. Mod. Phys. **85**, 79 (2013).

[40] P. Machnikowski, K. Gawarecki, and Ł. Cywiński, Hyperfine interaction for holes in quantum dots: $k \cdot p$ Model, Phys. Rev. B **100**, 085305 (2019).

[41] E. A. Chekhovich, M. M. Glazov, A. B. Krysa, M. Hopkinson, P. Senellart, A. Lemaître, M. S. Skolnick, and A. I. Tartakovskii, Element-sensitive measurement of the hole–nuclear spin interaction in quantum dots, Nature Phys **9**, 74 (2013).

[42] I. D. Avdeev and D. S. Smirnov, Hyperfine interaction in atomically thin transition metal dichalcogenides, Nanoscale Adv. **1**, 2624 (2019).

[43] R. M. Martin, Elastic properties of ZnS structure semiconductors, Phys. Rev. B **1**, 4005 (1970).

[44] D. S. P. Tanner, M. A. Caro, S. Schulz, and E. P. O'Reilly, Fully analytic valence force field model for the elastic and inner elastic properties of diamond and zincblende crystals, Phys. Rev. B **100**, 094112 (2019).

[45] G. Bester, X. Wu, D. Vanderbilt, and A. Zunger, Importance of second-order piezoelectric effects in zinc-blende semiconductors, Phys. Rev. Lett. **96**, 187602 (2006).

[46] M. A. Caro, S. Schulz, and E. P. O'Reilly, Origin of nonlinear piezoelectricity in III-V semiconductors: Internal strain and bond ionicity from hybrid-functional density functional theory, Phys. Rev. B **91**, 075203 (2015).

[47] J. C. Slater and G. F. Koster, Simplified LCAO method for the periodic potential problem, Phys. Rev. **94**, 1498 (1954).

[48] M. Graf and P. Vogl, Electromagnetic fields and dielectric response in empirical tight-binding theory, Phys. Rev. B **51**, 4940 (1995).

[49] T. B. Boykin and P. Vogl, Dielectric response of molecules in empirical tight-binding theory, Phys. Rev. B **65**, 035202 (2001).

[50] P. Vogl and C. Strahberger, Self-similar optical absorption spectra in high magnetic fields, phys. stat. sol. (b) **234**, 472 (2002).

[51] X. Ma, G. W. Bryant, and M. F. Doty, Hole spins in an InAs/GaAs quantum dot molecule subject to lateral electric fields, Phys. Rev. B **93**, 245402 (2016).

[52] R. Benchamekh, F. Raouafi, J. Even, F. Ben Cheikh Larbi, P. Voisin, and J.-M. Jancu, Microscopic electronic wave function and interactions between quasiparticles in empirical tight-binding theory, Phys. Rev. B **91**, 045118 (2015).

[53] J.-M. Jancu, R. Scholz, F. Beltram, and F. Bassani, Empirical tight-binding calculation for cubic semiconductors: General method and material parameters, Phys. Rev. B **57**, 6493 (1998).

[54] J.-M. Jancu and P. Voisin, Tetragonal and trigonal deformations in zinc-blende semiconductors: A tight-binding point of view, Phys. Rev. B **76**, 115202 (2007).

[55] Y. M. Niquet, D. Rideau, C. Tavernier, H. Jaouen, and X. Blase, Onsite matrix elements of the tight-binding Hamiltonian of a strained crystal: Application to silicon, germanium, and their alloys, Phys. Rev. B **79**, 245201 (2009).

[56] K. Gawarecki and M. Zieliński, Electron *g* factor in nanostructures: Continuum media and atomistic approach, Sci. Rep. **10**, 22001 (2020).

[57] R. Winkler, *Spin-Orbit Coupling Effects in Two-Dimensional Electron and Hole Systems* (Springer, New York, 2003).

[58] H. R. Trebin, U. Rössler, and R. Ranvaud, Quantum resonances in the valence bands of zinc-blende semiconductors. I. Theoretical aspects, Phys. Rev. B **20**, 686 (1979).

[59] G. Yong-Xian, Y. Tao, J. Hai-Ming, X. Peng-Fei, and W. Zhan-Guo, Impact of symmetrized and Burt–Foreman Hamiltonians on spurious solutions and energy levels of InAs/GaAs quantum dots, Chinese Phys. B **19**, 088102 (2010).

[60] G. L. Bir and G. E. Pikus, *Symmetry and Strain-Induced Effects in Semiconductors* (Wiley, New York, 1974).

[61] K. Suzuki and J. C. Hensel, Quantum resonances in the valence bands of germanium. I. Theoretical considerations, Phys. Rev. B **9**, 4184 (1974).

[62] K. Gawarecki and M. Zieliński, Importance of second-order deformation potentials in modeling of InAs/GaAs nanostructures, Phys. Rev. B **100**, 155409 (2019).

[63] M. Krzykowski, K. Gawarecki, and P. Machnikowski, Hole spin-flip transitions in a self-assembled quantum dot, Phys. Rev. B **102**, 205301 (2020).

[64] A. Mielnik-Pyszczorski, K. Gawarecki, and P. Machnikowski, Limited accuracy of conduction band effective mass equations for semiconductor quantum dots, Sci. Rep. **8**, 2873 (2018).

[65] I. Žutić, J. Fabian, and S. Das Sarma, Spintronics: Fundamentals and applications, Rev. Mod. Phys. **76**, 323 (2004).

[66] A. V. Khaetskii and Y. V. Nazarov, Spin relaxation in semiconductor quantum dots, Phys. Rev. B **61**, 12639 (2000).

[67] A. V. Khaetskii and Y. V. Nazarov, Spin-flip transitions between Zeeman sublevels in semiconductor quantum dots, Phys. Rev. B **64**, 125316 (2001).

[68] A. Mielnik-Pyszczorski, K. Gawarecki, M. Gawełczyk, and P. Machnikowski, Dominant role of the shear strain induced admixture in spin-flip processes in self-assembled quantum dots, Phys. Rev. B **97**, 245313 (2018).

[69] M. Gawełczyk and K. Gawarecki, Tunneling-related electron spin relaxation in self-assembled quantum-dot molecules, Phys. Rev. B **103**, 245422 (2021).

[70] T. Andlauer, R. Morschl, and P. Vogl, Gauge-invariant discretization in multiband envelope function theory and g factors in nanowire dots, Phys. Rev. B **78**, 075317 (2008).

[71] T. Eissfeller and P. Vogl, Real-space multiband envelope-function approach without spurious solutions, Phys. Rev. B **84**, 195122 (2011).

[72] T. Eissfeller, Theory of the electronic structure of quantum dots in external fields, Ph.D. thesis, Technical University of Munich, 2012.

[73] H. Haken, *Quantum Field Theory of Solids: An Introduction* (Amsterdam, New York, 1976).

[74] H. Haug and S. Koch, *Quantum Theory of the Optical and Electronic Properties of Semiconductors* (World Scientific, New Jersey, 2009).

[75] J. Andrzejewski, G. Sęk, E. O'Reilly, A. Fiore, and J. Misiewicz, Eight-band $k \cdot p$ calculations of the composition contrast effect on the linear polarization properties of columnar quantum dots, J. Appl. Phys. **107**, 073509 (2010).

[76] R. P. Feynman, Forces in molecules, Phys. Rev. **56**, 340 (1939).

[77] L. C. Lew Yan Voon and L. R. Ram-Mohan, Tight-binding representation of the optical matrix elements: Theory and applications, Phys. Rev. B **47**, 15500 (1993).

[78] A. Thränhardt, C. Ell, G. Khitrova, and H. M. Gibbs, Relation between dipole moment and radiative lifetime in interface fluctuation quantum dots, Phys. Rev. B **65**, 035327 (2002).

[79] A. H. Kachare, W. G. Spitzer, and J. E. Fredrickson, Refractive index of ion-implanted gaas, J. Appl. Phys. **47**, 4209 (1976).

[80] C. Testelin, F. Bernardot, B. Eble, and M. Chamarro, Hole–spin dephasing time associated with hyperfine interaction in quantum dots, Phys. Rev. B **79**, 195440 (2009).

[81] P. Podemski, A. Musiał, K. Gawarecki, A. Maryński, P. Gontar, A. Bercha, W. A. Trzeciakowski, N. Srocka, T. Heuser, D. Quandt, A. Strittmatter, S. Rodt, S. Reitzenstein, and G. Sęk, Interplay between emission wavelength and s-p splitting in MOCVD-grown InGaAs/GaAs quantum dots emitting above 1.3 μm, Appl. Phys. Lett. **116**, 023102 (2020).

[82] C. E. Pryor and M. E. Flatté, Landé g factors and orbital momentum quenching in semiconductor quantum dots, Phys. Rev. Lett. **96**, 026804 (2006).

[83] J. van Bree, A. Yu. Silov, M. L. Van Maasakkers, C. E. Pryor, M. E. Flatté, and P. M. Koenraad, Anisotropy of electron and hole g tensors of quantum dots: An intuitive picture based on spin-correlated orbital currents, Phys. Rev. B **93**, 035311 (2016).

[84] L. Jacak, A. Wójs, and P. Hawrylak, *Quantum dots* (Berlin, Heidelberg, 1998).

[85] B. Kramer and A. MacKinnon, Localization: Theory and experiment, Rep. Prog. Phys. **56**, 1469 (1993).

[86] *Topics in Applied Physics*, edited by P. Michler (Springer, New York, 2003), Vol. 90.

[87] E. J. O'Halloran, C. A. Broderick, D. S. P. Tanner, S. Schulz, and E. P. O'Reilly, Comparison of first principles and semi-empirical models of the structural and electronic properties of $\mathrm{Ge}_{1-x}\mathrm{Sn}_x$ alloys, Opt. Quantum Electron. **51**, 314 (2019).

[88] S. Balay, S. Abhyankar, M. F. Adams, S. Benson, J. Brown, P. Brune, K. Buschelman, E. M. Constantinescu, L. Dalcin, A. Dener, V. Eijkhout, J. Faibussowitsch, W. D. Gropp, V. Hapla, T. Isaac, P. Jolivet, D. Karpeev, D. Kaushik, M. G. Knepley, F. Kong *et al.*, PETSc web page (2024), https://petsc.org/.

[89] I. Vurgaftman, J. R. Meyer, and L. R. Ram-Mohan, Band parameters for III-V compound semiconductors and their alloys, J. Appl. Phys. **89**, 5815 (2001).

[90] S. Birner, Modeling of semiconductor nanostructures and semiconductor–electrolyte interfaces, Ph.D. thesis, Technical University of Munich, 2011.

[91] J. S. Blakemore, Semiconducting and other major properties of gallium arsenide, J. Appl. Phys. **53**, R123 (1982).

[92] Y. Lacroix, C. A. Tran, S. P. Watkins, and M. L. W. Thewalt, Low-temperature photoluminescence of epitaxial InAs, J. Appl. Phys. **80**, 6416 (1996).

[93] C. Hermann and C. Weisbuch, $\vec{\mathrm{k}} \cdot \vec{\mathrm{p}}$ perturbation theory in III-V compounds and alloys: A reexamination, Phys. Rev. B **15**, 823 (1977).

[94] L. G. Shantharama, A. R. Adams, C. N. Ahmad, and R. J. Nicholas, The k.p interaction in InP and GaAs from the band-gap dependence of the effective mass, J. Phys. C: Solid State Phys. **17**, 4429 (1984).

[95] L. M. Kanskaya, S. I. Kokhanovskii, R. P. Seisyan, Al. L. Efros, and V. A. Yukish, Magneto-optical study of excitons in GaAs in high magnetic fields, Sov. Phys. Semicond. **17**, 449 (1983).

[96] D. E. Aspnes and A. A. Studna, Schottky-Barrier electroreflectance: Application to GaAs, Phys. Rev. B **7**, 4605 (1973).

[97] N. Ahmed, I. R. Agool, M. G. Wright, K. Mitchell, A. Koohian, S. J. A. Adams, C. R. Pidgeon, B. C. Cavenett, C. R. Stanley, and A. H. Kean, Far-infrared optically detected cyclotron resonance in gaas layers and low-dimensional structures, Semicond. Sci. Technol. **7**, 357 (1992).

[98] P. Lawaetz, Valence-Band parameters in cubic semiconductors, Phys. Rev. B **4**, 3460 (1971).

[99] C. G. Van De Walle, Band lineups and deformation potentials in the model-solid theory, Phys. Rev. B **39**, 1871 (1989).

[100] See Supplemental Material at http://link.aps.org/supplemental/10.1103/vjrj-jc3c for material parameters and source data supporting the figures.

[101] M. Frigo and S. Johnson, The design and implementation of FFTW3, Proc. IEEE **93**, 216 (2005).

[102] A. H. Barnett, J. Magland, and L. af Klinteberg, A parallel nonuniform fast fourier transform library based on an "exponential of semicircle" kernel, SIAM J. Sci. Comput. **41**, C479 (2019).

[103] A. H. Barnett, Aliasing error of the $\exp(\beta\sqrt{1-z^2})$ kernel in the nonuniform fast fourier transform, Appl. Comput. Harmon. Anal. **51**, 1 (2021).

[104] J.-Y. Lee and L. Greengard, The type 3 nonuniform FFT and its applications, J. Comput. Phys. **206**, 1 (2005).